



**HAL**  
open science

## Dynamic regimes in planetary cores: $\tau$ - $\ell$ diagrams

Henri-Claude Nataf, Nathanaël Schaeffer

► **To cite this version:**

Henri-Claude Nataf, Nathanaël Schaeffer. Dynamic regimes in planetary cores:  $\tau$ - $\ell$  diagrams. 2023.  
hal-04135499

**HAL Id: hal-04135499**

**<https://hal.science/hal-04135499>**

Preprint submitted on 3 Jul 2023

**HAL** is a multi-disciplinary open access archive for the deposit and dissemination of scientific research documents, whether they are published or not. The documents may come from teaching and research institutions in France or abroad, or from public or private research centers.

L'archive ouverte pluridisciplinaire **HAL**, est destinée au dépôt et à la diffusion de documents scientifiques de niveau recherche, publiés ou non, émanant des établissements d'enseignement et de recherche français ou étrangers, des laboratoires publics ou privés.



Distributed under a Creative Commons Attribution - NonCommercial - NoDerivatives 4.0  
International License



---

# Dynamic regimes in planetary cores: $\tau$ - $\ell$ diagrams

## *Régimes dynamiques dans les noyaux planétaires : diagrammes $\tau$ - $\ell$*

Henri-Claude Nataf<sup>®</sup>\*,<sup>a</sup> and Nathanaël Schaeffer<sup>®</sup> <sup>a</sup>

<sup>a</sup> Univ. Grenoble Alpes, Univ. Savoie Mont Blanc, CNRS, IRD, Univ. Gustave Eiffel, ISTERre, 38000 Grenoble, France

*E-mails:* Henri-Claude.Nataf@univ-grenoble-alpes.fr (H.-C. Nataf),  
Nathanael.Schaeffer@univ-grenoble-alpes.fr (N. Schaeffer)

**Abstract.** Planetary cores are the seat of rich and complex fluid dynamics, in which the effects of rotation and magnetic field combine. The equilibria governing the strength of the magnetic field produced by the dynamo effect, the organisation and amplitude of the flow, and those of the density field, remain debated despite remarkable progress made in their numerical simulation. This paper proposes a new approach based on the explicit consideration of the variation of time scales  $\tau$  with spatial scales  $\ell$  for the different physical phenomena involved. The  $\tau$ - $\ell$  diagrams thus constructed constitute a very complete graphic summary of the dynamics of the object under study. They reveal the domains of validity of the different possible dynamic regimes. Several scenarios are thus constructed and discussed for the Earth's core, shedding new light on the width of convective columns and on the force equilibria to be considered. A QG-MAC scenario adapted from Aubert [2019] gives a good account of the observations. A diversion to Venus reveals the subtlety and relativity of the notion of 'fast rotator'. A complete toolbox is provided, allowing everyone to construct a  $\tau$ - $\ell$  diagram of a numerical simulation, a laboratory experiment, a theory, or a natural object.

Supplementary material for this article is supplied as a separate archive Nataf\_Schaeffer\_SupMat.zip, the related data is displayed in document Nataf\_Schaeffer\_SupMat.pdf.

**Résumé.** Les noyaux planétaires sont le siège d'une dynamique des fluides riche et complexe où se combinent les effets de la rotation et du champ magnétique. Les équilibres gouvernant l'intensité du champ magnétique produit par effet dynamo, l'organisation et l'amplitude de l'écoulement, et celles du champ de densité, demeurent débattus, malgré les progrès remarquables de leur simulation numérique. Cet article propose une nouvelle approche qui repose sur la prise en compte explicite de la variation des échelles de temps  $\tau$  avec les échelles spatiales  $\ell$  pour les différents phénomènes physiques impliqués. Les diagrammes  $\tau$ - $\ell$  ainsi construits constituent un résumé graphique très complet de la dynamique de l'objet étudié. Ils révèlent les domaines de validité des différents régimes dynamiques possibles. Plusieurs scénarios sont ainsi construits et discutés pour le noyau terrestre, apportant un nouvel éclairage sur la largeur des colonnes convectives et sur les équilibres de force à considérer. Un scénario QG-MAC adapté de Aubert [2019] rend bien compte des observations. Un détour par Vénus révèle la subtilité et la relativité de la notion de 'rotateur rapide'. Une boîte à outils complète est fournie, permettant à chacun de construire le diagramme  $\tau$ - $\ell$  d'une simulation numérique, d'une expérience de laboratoire, d'une théorie, ou d'un objet naturel.

---

\* Corresponding author.

**Keywords.** Turbulence, tau-ell, Dynamo, Core, Convection.

This article is a draft (not yet accepted!)

## 1. Introduction

Enormous progress has been achieved in the modeling and understanding of the magnetic dynamo at work in the core of the Earth and other planets since the first 3D numerical simulations of Glatzmaier and Roberts [1995] and Kageyama et al. [1995]. It rapidly appeared that the magnetic fields produced by such numerical simulations met the main characteristics of the long-term magnetic field observed on Earth, such as its dipolarity, the presence of high-flux patches at high latitudes, and symmetry properties [Christensen et al., 1999, Olson and Christensen, 2006, Christensen et al., 2010]. Magnetic intensity scaling laws for planetary and stellar dynamos were obtained by combining an analysis of the dominant terms of the governing equations with results of an extensive survey of numerical simulations [Christensen and Aubert, 2006, Christensen, 2010].

In the meantime, shorter timescale manifestations of the geodynamo were unveiled, such as a large-scale off-centered anticyclone [e.g., Pais and Jault, 2008], and torsional waves (geostrophic Alfvén waves) with periods of a few years [Gillet et al., 2010]. These new observations prompted efforts to run numerical simulations at more extreme parameter values [Schaeffer et al., 2017, Aubert et al., 2017], increasing the role of rotation by decreasing the Ekman number down to  $Ek = 10^{-7}$ , and increasing the convective forcing up to  $Ra/Ra_c = 6300$ , where  $Ra$  is the Rayleigh number, and  $Ra_c$  its critical value. These extreme simulations of the geodynamo successfully account for fast dynamics retrieved from observations.

In view of this remarkable progress, it might seem that most problems are solved. In fact, hot debates are still roaming on several crucial issues. One of them concerns the dominant length-scale of convective structures in Earth's core. Column widths of 100 m are suggested by Yan and Calkins [2022] while Guervilly et al. [2019] advocate 30 km. Extrapolating force-balances from numerical simulations and laboratory experiments to natural systems is another issue [Aurnou and King, 2017, Schwaiger et al., 2019, Teed and Dormy, 2023]. The relevance of scenarios with weak and strong magnetic field branches is also hotly debated [Dormy, 2016]. One extreme viewpoint being expressed by Cattaneo and Hughes [2022] who claim that Earth would not have been able to produce a strong magnetic field as today without Moon's help.

There is room for such diverging views because the distance from numerically accessible parameters to expected planetary values remains vertiginous. Laboratory experiments somewhat enlarge the accessible range but are limited to non-dynamo regimes, making the link with numerics and observations difficult.

This is the motivation for exploring a different route: instead of extrapolating available simulations to core conditions, start from the actual expected properties of the core, and patch scenarios of turbulence that correspond to different regimes encountered at different scales. This leads to the construction of  $\tau$ - $\ell$  regime diagrams of turbulence, as introduced by Nataf and Schaeffer [2015].

Our experience is that this approach is an excellent intuition-booster. It provides a simple graphical support that can greatly help deciphering and testing more mathematically-motivated approaches. However, we consider that it has not received enough attention, perhaps because it clearly advocates a 'fuzzy physics' method, and also because it was originally published in a limited-access collection.

In this article, we present an improved version of  $\tau$ - $\ell$  regime diagrams. We detail the steps for constructing such diagrams, providing examples of application to numerical simulations and laboratory experiments. Key properties of  $\tau$ - $\ell$  diagrams are highlighted and illustrated by simple examples.

The central part of the article is devoted to an application to the Earth's core. We propose scenarios for a non-magnetic rotating convective core, and for a dynamo-generating rotating convective core. The resulting diagrams are compared with the predictions of several scaling analyses [Christensen and Aubert, 2006, Christensen, 2010, Davidson, 2013, Aubert et al., 2017].

One important novelty is that our  $\tau$ - $\ell$  diagrams are constructed to satisfy a given constraint on the convective power available to drive the dynamo. Indeed, planets are thermal machines and their thermal evolution is probably what we can estimate best. Liquid cores of planets cool down on geological timescales, generating convective motions. Convective power, which can be estimated from the planet's thermal history [*e.g.*, Stevenson et al., 1983, Lister, 2003, Nimmo, 2015, Landeau et al., 2022, Driscoll and Davies, 2023], sustains fluid flow and magnetic field. Dissipation of this power by either momentum or magnetic diffusion, or both, controls the regimes of turbulence the system experiences. This should facilitate the construction of  $\tau$ - $\ell$  diagrams for planets, exoplanets and stars for which no direct observation of the large-scale flow velocity and magnetic field is available.

We present and illustrate the construction rules and key properties of  $\tau$ - $\ell$  regime diagrams of turbulence in Section 2. Section 3 introduces the physical phenomena at work in planetary cores, and relates  $\tau$ - $\ell$  diagrams to classical dimensionless numbers. Section 4 presents  $\tau$ - $\ell$  regime diagrams for a non-magnetic core.  $\tau$ - $\ell$  diagrams of the present-day geodynamo are built in Section 5 and discussed in Section 6. Limitations and perspectives are outlined in Section 7, and we conclude in Section 8. Appendices A and B provide rules for converting spectra and force balances in  $\tau$ - $\ell$  language. Simple Python programs used to build  $\tau$ - $\ell$  diagrams are given as supplementary material, together with additional examples from numerical simulations and laboratory experiments.

## 2. Construction rules and key properties of $\tau$ - $\ell$ diagrams

This section presents the rules used to construct  $\tau$ - $\ell$  diagrams. Turbulent systems display a wide range of length-scales and timescales. Timescales of physical phenomena such as diffusion or wave propagation depend upon the length-scale at which they operate. For example, timescale  $\tau_v$  of momentum diffusion at length-scale  $\ell$  can be written as  $\tau_v(\ell) = \ell^2/\nu$ . Similarly, turnover time  $\tau_u$  of a vortex of radius  $\ell$  is given by  $\tau_u(\ell) = \ell/u(\ell)$ , where  $u(\ell)$  is the vortex fluid velocity. We build  $\tau$ - $\ell$  regime diagrams by plotting timescales  $\tau_x$  as a function of length-scale  $\ell$  in a log-log plot, for all the different physical phenomena  $x$  that govern the fluid flow in a given system.

### Construction rules of $\tau$ - $\ell$ regime diagrams

$\tau$ - $\ell$  regime diagrams are 'object-oriented'. They are built following these steps:

- Identify physical phenomena that play an important role in the object under study.
- Document relevant physical properties (viscosity, thermal diffusivity, rotation rate, etc).
- Build and draw lines  $\tau(\ell)$  that control dissipative and wave propagation phenomena.
- Identify different turbulence regimes the object might experience.
- Construct and draw lines  $\tau(\ell)$  of fields (velocity, buoyancy, magnetic field) that describe the object's turbulent behaviour, given a dissipated power  $\mathcal{P}_{diss}$ .
- Compare predictions with observables such as large-scale flow velocity and magnetic field, when available.

### 2.1. A simple example: Kolmogorov's universal turbulence

We present the  $\tau$ - $\ell$  diagram of Kolmogorov's universal turbulence [Kolmogorov, 1941] in Figure 1 to illustrate the construction of  $\tau$ - $\ell$  diagrams. With applications to the dynamics of the Earth's core in mind, we consider a range of length-scales from 1 cm to  $R_o = 3480$  km, the radius of the core. Timescales span a range from 10 s to 32 000 years.

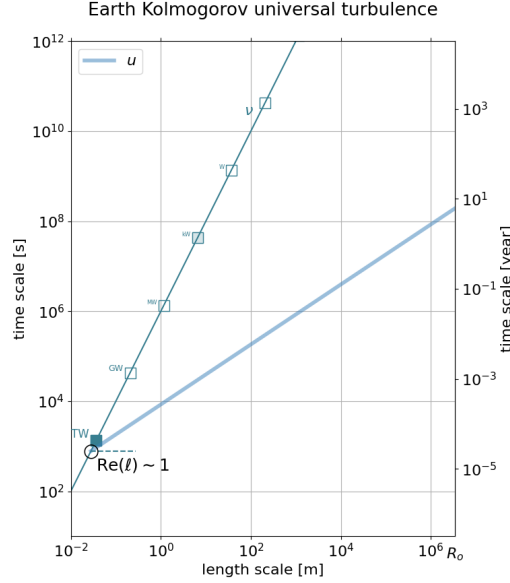


**Figure 1.**  $\tau$ - $\ell$  regime diagram for Kolmogorov’s universal turbulence [Kolmogorov, 1941]. Teal line labeled  $v$  is viscous dissipation line  $\tau_v(\ell) = \ell^2/\nu$ . Thick blue line is eddy turnover time  $\tau_u(\ell) = \epsilon^{-1/3} \ell^{2/3}$  inferred from Kolmogorov’s law, assuming that energy is injected at core radius length-scale  $\ell = R_o$ . Intersection of these two lines occurs for  $\text{Re}(\ell) \sim 1$  and is marked by a circle. Total energy dissipation rate  $\mathcal{P}_{diss}$  can be read at this intersection (horizontal dashed line), using square markers drawn and labelled along the viscous line. Markers are a factor of  $10^3$  apart, the 1 TW marker being filled.

### 2.1.1. $\tau_v(\ell)$ line

We pick a viscosity value  $\nu = 10^{-6} \text{ m}^2 \text{ s}^{-1}$  and draw the  $\tau_v(\ell)$  viscous dissipation line:

$$\tau_v(\ell) = \ell^2/\nu. \quad (1)$$

### 2.1.2. $\tau_u(\ell)$ line

In Kolmogorov’s universal turbulence, kinetic energy cascades down from large length-scales to small-scales, from the energy injection scale down to the viscous dissipation scale. The range in between is called the inertial range. The kinetic energy density spectrum  $E(k)$  in the inertial range obeys Kolmogorov’s law:

$$E(k) = C_K \epsilon^{2/3} k^{-5/3}, \quad (2)$$

where  $k$  is the wavenumber,  $\epsilon$  is the energy injection rate per unit mass, and  $C_K$  is Kolmogorov’s dimensionless constant, of order 1.

To build line  $\tau_u(\ell)$ , we need to convert kinetic energy density into velocity. It is common to define an ‘eddy turnover time’ as  $\tau_u(\ell) = \ell/u(\ell)$ , with  $u^2(\ell) \sim E(k)k$  and  $\ell \sim 1/k$  (see Appendix A.1). This translates into:

$$\tau_u(\ell) \simeq \ell^{3/2} [E(\ell^{-1})]^{-1/2}. \quad (3)$$

Dropping prefactor  $C_K$ , Kolmogorov’s law yields:

$$\tau_u(\ell) \simeq \epsilon^{-1/3} \ell^{2/3}. \quad (4)$$

We draw this  $\tau_u(\ell)$  line in Figure 1, assuming that the energy injection length-scale is  $R_o$ , and choosing an injection timescale, which will be discussed later. Note that we will use another rule to convert energy spectra into  $\tau_u(\ell)$  in the rest of this article, as explained in Appendix A.

### 2.1.3. $\ell$ -scale Reynolds number

We terminate line  $\tau_u(\ell)$  where it hits viscous line  $\tau_v(\ell)$ . This intersection yields Kolmogorov microscales  $(\ell_K, \tau_K)$ , for which  $\tau_u(\ell_K) = \ell_K^2/\nu$ , i.e.,  $\frac{u(\ell_K)\ell_K}{\nu} = 1$ . Defining an  $\ell$ -scale Reynolds number  $Re(\ell) = \frac{u(\ell)\ell}{\nu}$ , we note that the intersection of the eddy turnover time line  $\tau_u(\ell)$  with the viscous line  $\tau_v(\ell)$  occurs at  $Re(\ell) = 1$ . It marks the transition from the inertial cascade at large scale to the viscous dissipation regime at small scale.

### 2.1.4. Power dissipation markers

In Kolmogorov's theory, the energy injected at large scale cascades down with no loss to small scales at which viscous dissipation takes place. This dissipation range starts at the intersection of lines  $\tau_u$  and  $\tau_v$ , where  $Re(\ell) \sim 1$ , which defines Kolmogorov microscales  $(\ell_K, \tau_K)$ . From equations (1) and (4), we deduce:

$$\epsilon = \frac{\ell_K^2}{\tau_K^3} = \frac{\nu}{\tau_K^2} = \frac{u^2(\ell_K)}{\tau_K}, \quad (5)$$

where the last expression shows that dissipation rate per unit mass  $\epsilon$  equals kinetic energy at the microscale divided by eddy turnover time at that scale. We also see that we can attribute to each  $\tau_v$  value a dissipation rate per unit mass. Multiplying by the mass of the system, we obtain the total dissipated power. In Figure 1, we thus draw power markers along the viscous dissipation line, using the mass of the outer core  $M_o = 1.835 \cdot 10^{24}$  kg. Markers are a factor of one thousand apart and are labeled.

### 2.1.5. Energy

In Kolmogorov's universal turbulence, kinetic energy is dominated by large length-scales. In  $\tau$ - $\ell$  diagrams, we retrieve kinetic energy  $\mathcal{E}$  from the square of the inverse of  $\tau_u(R_o)$  since:

$$\mathcal{E} = \frac{1}{2} \int_{V_o} \rho U^2 dV \sim M_o u^2(R_o) = \frac{M_o R_o^2}{\tau_u^2(R_o)}, \quad (6)$$

where  $V_o$  is the volume of the liquid core. We use this property to compare the amplitudes of the various energy reservoirs when dealing with planetary cores. Note that this applies as long as the  $\tau_u(\ell)$  slope is less than 1, in order for large-scale energy to dominate.

#### Key properties of $\tau$ - $\ell$ regime diagrams

- $\tau$ - $\ell$  regime diagrams gather in a simple graphical representation many of the ingredients that control the dynamics of a turbulent fluid system.
- In  $\tau$ - $\ell$  regime diagrams, intersections of lines  $\tau_x(\ell)$  and  $\tau_y(\ell)$  of physical phenomena  $x$  and  $y$  occur where  $\ell$ -scale dimensionless number  $Z(\ell) = \frac{\tau_y(\ell)}{\tau_x(\ell)}$  equals 1. They mark a change in the system's dynamical regime.
- Usual integral-scale values of dimensionless numbers are obtained from the ratio of relevant  $\tau_x(\ell)$  and  $\tau_y(\ell)$  times at integral scale  $\ell = R_o$ .
- Total dissipated power can be marked along  $\tau(\ell)$  lines of dissipative phenomena.
- Energies of different types (kinetic, gravitational, magnetic) are represented by the inverse square of corresponding  $\tau(R_o)$ .
- $\tau$ - $\ell$  regime diagrams are a useful tool to infer or test turbulence scenarios. They are *not* a theory of turbulence.

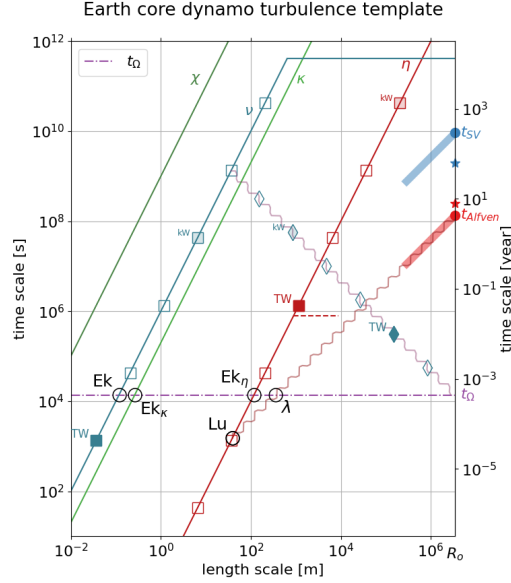


**Figure 2.**  $\tau$ - $\ell$  regime diagram template for the Earth's core. Wavy lines pinned to  $t_\Omega$  and to  $t_{Alfven}$  are  $\tau_{Rossby}(\ell)$  and  $\tau_{Alfven}(\ell)$ , respectively. Their expressions are given in Table I, together with those of diffusion lines labeled  $\chi$ ,  $\nu$ ,  $\kappa$  and  $\eta$ . Thick lines pinned to  $t_{SV}$  and  $t_{Alfven}$  along right  $y$ -axis mark large-scale observed values and trends of core flow and magnetic field, respectively. Property values used to draw the diagram are given in Table II. Markers along lines  $\tau_\nu$ ,  $\tau_{Rossby}$  and  $\tau_\eta$  indicate power dissipation. Markers are a factor of 1000 apart, the 1 TW marker being filled. Circles labeled Ek,  $Ek_\kappa$ ,  $Ek_\eta$ , Lu and  $\lambda$  at line intersections mark scales at which the corresponding  $\ell$ -scale dimensionless number (see Table III) equals 1.

### 3. Physical phenomena in planetary cores and dimensionless numbers

We now turn our attention to planetary cores. Flow within planetary cores are mostly powered by thermal or thermo-compositional convection. They often produce a magnetic field. Most importantly, these flows occur in a rotating spherical system.

In this section, we introduce the  $\tau$ - $\ell$  lines these physical phenomena contribute. We illustrate the resulting  $\tau$ - $\ell$  regime diagram template, using values pertaining to Earth's core, and relate the diagram to various dimensionless numbers used to characterize planetary core dynamics.

#### 3.1. Physical phenomena and their $\tau$ - $\ell$ expressions

Table I gives the expressions of major  $\tau(\ell)$  times pertaining to planetary cores.  $\tau_\nu(\ell)$  and  $\tau_u(\ell)$  times have been introduced in section 2.1. Convection adds thermal diffusion and buoyancy scales. Rotation, spherical boundaries, and magnetic field contribute key additional timescales.

We discuss the origin and meaning of these various  $\tau(\ell)$  scales, and illustrate the  $\tau$ - $\ell$  template they provide in Earth's core example (Figure 2), using its properties listed in Table II.

time	expression	phenomenon
$\tau_\nu(\ell)$	$\ell^2/\nu$	viscous dissipation
$\tau_\kappa(\ell)$	$\ell^2/\kappa$	thermal diffusion
$\tau_\chi(\ell)$	$\ell^2/\chi$	compositional diffusion
$\tau_\eta(\ell)$	$\ell^2/\eta$	magnetic dissipation
$t_\Omega$	$1/\Omega$	rotation
$\tau_{Rossby}(\ell)$	$R_o/\Omega\ell$	Rossby wave propagation
$\tau_{Alfven}(\ell)$	$\ell\sqrt{\rho\mu}/B_0$	Alfvén wave propagation
$\tau_\rho(\ell)$	$\sqrt{\frac{\ell}{g} \frac{\rho}{ \Delta\rho(\ell) }}$	buoyancy (or free-fall)
$\tau_u(\ell)$	$\ell/u(\ell)$	eddy turnover
$\tau_b(\ell)$	$\ell\sqrt{\rho\mu}/b(\ell)$	magnetic collision

**Table I.** Notation and expression of  $\tau(\ell)$  times of relevant physical phenomena for planetary cores. Fluid properties: density  $\rho$ ; kinematic viscosity  $\nu$ ; thermal and compositional diffusivities  $\kappa$  and  $\chi$ , respectively; magnetic diffusivity  $\eta$ ; magnetic permeability  $\mu$ . System properties: radius  $R_o$ ; gravity  $g$ ; rotation rate  $\Omega$ ; large-scale magnetic field  $B_0$ . Turbulent flow properties:  $\Delta\rho(\ell)$ ,  $u(\ell)$  and  $b(\ell)$  are  $\ell$ -scale density anomaly, eddy velocity, and magnetic field intensity, respectively. We also write  $\tau_\eta(R_o)$  as  $T_\eta$  for short. Adapted from Table 1 of Chapter 8.06 of *Treatise on Geophysics* [Nataf and Schaeffer, 2015] with permission.

symbol	value	unit	property
$\nu$	$10^{-6}$	$\text{m}^2 \text{s}^{-1}$	kinematic viscosity
$\kappa$	$5 \cdot 10^{-6}$	$\text{m}^2 \text{s}^{-1}$	thermal diffusivity
$\chi$	$10^{-9}$	$\text{m}^2 \text{s}^{-1}$	compositional diffusivity
$\eta$	1	$\text{m}^2 \text{s}^{-1}$	magnetic diffusivity
$\rho$	$10.9 \cdot 10^3$	$\text{kg m}^{-3}$	density
$\alpha$	$1.2 \cdot 10^{-5}$	$\text{K}^{-1}$	thermal expansion coefficient
$C_P$	850	$\text{J kg}^{-1} \text{K}^{-1}$	specific heat capacity
$R_o$	$3.48 \cdot 10^6$	m	core radius
$R_i$	$1.22 \cdot 10^6$	m	inner core radius
$M_o$	$1.835 \cdot 10^{24}$	kg	outer core mass
$g$	8	$\text{m s}^{-2}$	gravity
$t_\Omega$	$1.38 \cdot 10^4$	s	Earth's rotation time ( <i>i.e.</i> $1/2\pi$ day)
$\mathcal{P}_{diss}$	$3 \cdot 10^{12}$	W	available convective power
$t_{SV}$	$9 \cdot 10^9$	s	$R_o$ -scale core flow time ( <i>i.e.</i> $\approx 300$ years)
$t_{Alfven}$	$1.4 \cdot 10^8$	s	$R_o$ -scale Alfvén wave time ( <i>i.e.</i> $\approx 4$ years)

**Table II.** Properties of Earth's core. See Olson [2015] for details and uncertainties. Adapted from Table 3 of Chapter 8.06 of *Treatise on Geophysics* [Nataf and Schaeffer, 2015] with permission.



### 3.1.1. diffusion

Timescales of diffusive phenomena all share the same form  $\tau(\ell) = \ell^2/D$ , where diffusivity  $D$  is  $\nu$ ,  $\kappa$ ,  $\chi$  or  $\eta$  depending upon which field diffuses: momentum, temperature, composition or magnetic field, respectively.

### 3.1.2. convection

We introduce a ‘buoyancy’ or ‘free-fall’ timescale  $\tau_\rho(\ell) = \sqrt{\frac{\ell}{g} \frac{\rho}{|\Delta\rho(\ell)|}}$ , which is the time it takes for a parcel of fluid with density anomaly  $\Delta\rho(\ell)$  to rise or sink a distance  $\ell$  in the absence of diffusion.  $\tau_\rho(\ell)$  relates to density anomaly  $\Delta\rho$  at length-scale  $\ell$ . Density anomaly, flow velocity and magnetic field constitute the three fields for which we seek an adequate turbulent description.

We have shown in section 2.1 that the value of  $\tau_u$  at integral scale  $R_o$  measures the kinetic energy of the flow. Similarly, gravitational energy  $\mathcal{E}_g$  is measured by  $\tau_\rho(R_o)$  (as long as  $\tau_\rho(\ell)$  slope is less than 1) since:

$$\mathcal{E}_g = \frac{1}{2} \int_{V_o} g \Delta\rho r dV \sim M_o g R_o \frac{\Delta\rho(R_o)}{\rho} = \frac{M_o R_o^2}{\tau_\rho^2(R_o)}. \quad (7)$$

### 3.1.3. rotation

Rotation is a crucial ingredient of planetary core dynamics. It adds one important time in our  $\tau$ - $\ell$  regime diagram: the rotation time  $t_\Omega = \Omega^{-1}$ , *i.e.*, one day divided by  $2\pi$ . Physical phenomena operating at timescales smaller than  $t_\Omega$  are not influenced by planet’s spin, while those with longer timescales feel the effect of rotation. We thus draw a horizontal line at  $t_\Omega$  in the diagram of Figure 2. The intersection of this line with the viscous line yields Ekman layer’s thickness  $\ell_E = \sqrt{\nu/\Omega}$ . It is the only length-scale one can build from  $\nu$  and  $\Omega$  alone, and it controls friction, hence viscous dissipation, that takes place at boundaries. It turns out that boundaries bring up new important dynamical constraints and scales.

### 3.1.4. rotation and spherical boundaries

We will not review here the vast literature on rotating fluids in containers. The book of Greenspan [1968] remains amazingly central. At this stage, let us simply recall that Navier-Stokes equation reduces to *geostrophic equilibrium* when Coriolis acceleration dominates:

$$2\rho\Omega \times \mathbf{u} = -\nabla P, \quad (8)$$

where  $\mathbf{u}$  and  $P$  are fluid velocity and pressure, respectively. Taking the curl of this equation yields *Proudman-Taylor constraint*:

$$\frac{\partial \mathbf{u}}{\partial z} = 0, \quad (9)$$

where  $z$  coordinate is parallel to  $\Omega$ . Reintroducing acceleration term  $\rho \partial_t \mathbf{u}$  allows for the propagation of *inertial waves*.

Proudman-Taylor constraint would inhibit all fluid motions in a rotating fluid bounded by a solid container. *Quasi-geostrophic* (QG) fluid motions are instead observed, which approximately satisfy Proudman-Taylor constraint (*i.e.*,  $z$ -invariance) in the bulk (at least for one component, typically the azimuthal velocity), and connect to boundaries via thin *Ekman layers* in which viscous forces balance Coriolis.

It is important to note that Proudman-Taylor constraint is established by the propagation of inertial waves in the fluid, and is effective only when they had time to reach a boundary. Thus, a localized eddy of radius  $\ell$  grows into a columnar vortex at a speed equal to  $\Omega\ell$  [Davidson et al., 2006]. This means that large eddies rapidly form quasi-geostrophic columns, while it takes more time for small eddies to form core-size columns. Time for reaching quasi-geostrophy is thus given by:

$$\tau_{Rossby}(\ell) = \frac{R_o}{\Omega\ell}, \quad (10)$$

as written in Table I. This line is drawn as a wavy line in Figure 2. It is pinned to time  $t_\Omega$  at  $\ell = R_o$ , and we extend it until it reaches viscous line  $\tau_\nu(\ell)$ .

Note that  $\tau_{Rossby}(\ell)$  also equals the time it takes for a Rossby wave of wavelength  $\ell$  to propagate one wavelength (hence its name) [Nataf and Schaeffer, 2015]. The intersection of the  $\tau_u(\ell)$  line with the Rossby line has  $\ell = \sqrt{u(\ell)}/\Omega$ , which defines a *Rhines scale* (originally more precisely defined as  $\ell = \sqrt{u}/\beta$ , where  $\beta = 2\Omega \sin\theta/R_o$  is the northward gradient of Coriolis frequency at colatitude  $\theta$  [Rhines, 1975]).

Flow is quasi-geostrophic for scales above  $\tau_{Rossby}$  line. In the triangle formed by Rossby, viscous and  $t_\Omega$  lines, flow structures are elongated parallel to spin axis but not enough to reach both boundaries. Flow is 3D beneath  $t_\Omega$  line.

### 3.1.5. Quasi-geostrophic dissipation

Quasi-geostrophic vortices dissipate kinetic energy by Ekman friction at boundaries of the liquid core. We approximate energy loss rate  $p_\ell$  of a single QG vortex of radius  $\ell$  by:

$$p_\ell = \rho\nu \frac{u^2(\ell)}{\ell_E^2} \ell_E \ell^2. \quad (11)$$

Summing contributions of all  $\ell$ -scale QG vortices filling the entire core, we obtain the total power dissipated by Ekman friction  $P_{QG}$ . Dividing by the mass of the core, we obtain the QG viscous dissipation rate per unit mass  $\epsilon_{QG}$  at  $\ell$ -scale as:

$$\epsilon_{QG} = \nu \frac{u^2(\ell)}{R_o \ell_E} \quad (12)$$

Ekman friction matters for QG vortices. We therefore draw the corresponding power markers on the Rossby line, above which flow is quasi-geostrophic. Time  $\tau_{QG}$  for which total viscous dissipation by Ekman friction equals  $P_{QG}$  is then obtained from equation (12) as:

$$\tau_{QG} = \left[ \frac{M_o R_o}{P_{QG}} \sqrt{\frac{\nu}{\Omega^3}} \right]^{1/4}. \quad (13)$$

This provides markers drawn in Figure 2 as diamonds along Rossby line, a factor of one thousand apart, the TW marker being filled.

### 3.1.6. magnetic field, magnetic dissipation, magnetic energy

Magnetic fields are often produced and sustained by dynamo action within planetary cores. Presence of a magnetic field allows the propagation of magnetohydrodynamic waves called Alfvén waves [Alfvén, 1942]. In a uniform magnetic field  $B_0$ , these waves propagate at speed  $V_A = B_0/\sqrt{\rho\mu}$ , where  $\mu$  is fluid's magnetic permeability.

We construct time  $\tau_{Alfvén} = \ell \sqrt{\rho\mu}/B_0$ , the time it takes for an Alfvén wave to propagate distance  $\ell$ , with  $B_0$  the large-scale magnetic field. It is drawn as a red wavy line in Figure 2.

To describe magnetic field turbulent scales, we define a similar timescale, replacing  $B_0$  by  $\ell$ -scale magnetic field  $b(\ell)$ . Magnetic dissipation markers are labeled along  $\tau_\eta$  magnetic diffusion line, following the same rule as in equation (5).

Note that  $\tau_b(R_o) = \tau_{Alfvén}(R_o)$  provides the magnitude of magnetic energy  $\mathcal{E}_m$  (as long as  $\tau_b(\ell)$  slope is less than 1), since:

$$\mathcal{E}_m = \frac{1}{2\mu} \int_{V_o} B^2 dV \sim \frac{M_o}{\rho\mu} b^2(R_o) = \frac{M_o R_o^2}{\tau_b^2(R_o)}. \quad (14)$$

## 3.2. Dimensionless numbers

In order to connect to the huge literature pertaining to geophysical and astrophysical fluid dynamics, it is important to relate our  $\tau$ - $\ell$  regime diagrams to widely used dimensionless numbers. These numbers are dimensionless combinations of properties and field variables that appear when the equations governing the dynamics of the system under study are made dimensionless by normalizing their various terms by 'typical scales'.

number	expression	time ratio	name
$\text{Re}(\ell)$	$\frac{u(\ell)\ell}{\nu}$	$\frac{\tau_v(\ell)}{\tau_u(\ell)}$	Reynolds
$\text{Ra}(\ell)$	$\frac{g\ell^3 \Delta\rho(\ell) /\rho}{\kappa\nu}$	$\frac{\tau_\kappa(\ell)\tau_v(\ell)}{\tau_\rho^2(\ell)}$	Rayleigh
$\text{Ek}(\ell)$	$\frac{\nu}{\Omega\ell^2}$	$\frac{t_\Omega}{\tau_v(\ell)}$	Ekman
$\text{Ek}_\kappa(\ell)$	$\frac{\kappa}{\Omega\ell^2}$	$\frac{t_\Omega}{\tau_\kappa(\ell)}$	thermal Ekman
$\text{Ek}_\eta(\ell)$	$\frac{\eta}{\Omega\ell^2}$	$\frac{t_\Omega}{\tau_\eta(\ell)}$	magnetic Ekman
$\text{Ro}(\ell)$	$\frac{u(\ell)}{\Omega\ell}$	$\frac{t_\Omega}{\tau_u(\ell)}$	Rossby
$\text{Ro}_{ff}(\ell)$	$\frac{\sqrt{g\ell \Delta\rho(\ell) /\rho}}{\Omega\ell}$	$\frac{t_\Omega}{\tau_\rho(\ell)}$	free-fall Rossby
$\text{Rm}(\ell)$	$\frac{u(\ell)\ell}{\eta}$	$\frac{\tau_\eta(\ell)}{\tau_u(\ell)}$	magnetic Reynolds
$\text{Lu}(\ell)$	$\frac{\ell B_0}{\eta\sqrt{\rho\mu}}$	$\frac{\tau_\eta(\ell)}{\tau_{Alfven}(\ell)}$	Lundquist
$\Lambda(\ell)$	$\frac{b(\ell)B_0}{\rho\mu u(\ell)\Omega\ell}$	$\frac{\tau_u(\ell)t_\Omega}{\tau_b(\ell)\tau_{Alfven}(\ell)}$	Elsasser
$\lambda(\ell)$	$\frac{B_0}{\sqrt{\rho\mu}\Omega\ell}$	$\frac{t_\Omega}{\tau_{Alfven}(\ell)}$	Lehnert

**Table III.** Expressions of  $\ell$ -scale dimensionless numbers. These numbers are also expressed as ratios of characteristic  $\ell$ -scale times, which are defined in Table I. One recovers the classical expression of these numbers at integral scale by setting  $\ell = R_o$ . Adapted from Table 2 of Chapter 8.06 of *Treatise on Geophysics* [Nataf and Schaeffer, 2015] with permission.

For example, Reynolds number for a system of size  $L$  will be written:  $\text{Re} = \frac{UL}{\nu}$ , where  $U$  is a typical fluid velocity, and  $\nu$  kinematic viscosity. Usually, it is when this dimensionless number is of order 1 that a change of regime occurs. In this example: a change between a regime where momentum diffusion dominates over advection when  $\text{Re} < 1$  to one where advection dominates for  $\text{Re} > 1$ .

Most dimensionless numbers can be written as the ratio of two times. In our approach, we define length-scale dependent dimensionless numbers, constructed as the ratios of the timescales of the relevant physical phenomena. We thus define  $\ell$ -scale Reynolds number as:  $\text{Re}(\ell) = \frac{\tau_v(\ell)}{\tau_u(\ell)}$ , where  $\tau_v(\ell)$  is momentum diffusion timescale at length-scale  $\ell$ , while  $\tau_u(\ell)$  is the overturn time of a vortex of radius  $\ell$ . Table III gives the expressions of  $\ell$ -scale dimensionless numbers pertaining to planetary liquid core dynamics.

In  $\tau$ - $\ell$  regime diagrams, intersection of lines  $\tau_x(\ell)$  and  $\tau_y(\ell)$  of physical phenomena  $x$  and  $y$  occurs where  $\ell$ -scale dimensionless number  $Z(\ell) = \frac{\tau_y(\ell)}{\tau_x(\ell)}$  equals 1. Each such intersection marks a change in the system's dynamic regime.

In Figure 2, we have labeled several line intersections, where specific dimensionless numbers equal 1. The intersections of  $t_\Omega$  line and  $\nu$ ,  $\kappa$  and  $\eta$  lines indicate where corresponding  $\ell$ -scale Ekman numbers equal 1 in the  $\tau$ - $\ell$  plane. Intersection of Alfvén line and magnetic diffusion line defines where  $\ell$ -scale Lundquist number equals 1, marking a change from propagating Alfvén waves at larger scales to damped waves at smaller scales. Similarly, intersection of Alfvén line and  $t_\Omega$  line yields  $\lambda(\ell) \sim 1$ , where  $\lambda$  is Lehnert number [Lehnert, 1954, Jault, 2008]. System rotation favors quasi-geostrophic Alfvén waves at timescales above this intersection.

More dimensionless numbers, such as  $\text{Re}$ ,  $\text{Rm}$ ,  $\text{Ra}$ ,  $\text{Ro}$ ,  $\text{Ro}_{ff}$ , etc, will appear when we plot lines of system fields (buoyancy, velocity, magnetic field) for the different turbulence scenarios we will explore.

### 3.3. A word on Earth's core properties

Most properties listed in Table II are taken from Peter Olson's review in *Treatise on Geophysics* [Olson, 2015]. Some of them are known with great precision (to about 1% for core radius  $R_o$  and liquid core mass  $M_o$ ), but others are poorly constrained (to about 1 or 2 orders of magnitude for viscosity  $\nu$  and compositional diffusivity  $\chi$ ). In addition, most physical properties are expected to vary with radius. None of these (important) subtleties are taken into account in the 'fuzzy' approach we advocate for building  $\tau$ - $\ell$  regime diagrams. Note that we systematically drop all numerical prefactors, including  $2\pi$ .

As noted in section 1, power available to drive the dynamics of the system under study is a key ingredient. It largely controls the different turbulence regimes the system will experience. Thermal evolution of the Earth has received considerable attention (see Nimmo [2015], Landeau et al. [2022], Driscoll and Davies [2023] for reviews). It is now well established that the dynamics of Earth's core today is powered by its slow cooling, enhanced by the resulting growth of the solid inner core. As iron-nickel alloy crystallizes at its surface, it releases latent heat and light elements that drive convection and power the geodynamo.

Despite uncertainties on isentropic heat flux, the available convective power is found to be in the range  $0.8 - 5 \times 10^{12}$  W for present-day core [Nimmo, 2015, Landeau et al., 2022]. We adopt value  $\mathcal{P}_{diss} = 3$  TW.

Last two rows in Table II are not used to build  $\tau$ - $\ell$  diagrams, but instead to test their relevance. Large-scale vortex turnover time  $t_{SV} \approx 300$  years is retrieved from core flow inversions of magnetic secular variation [e.g., Pais and Jault, 2008]. Large-scale Alfvén wave propagation time  $t_{Alfven} \approx 4$  years is deduced from the discovery and analysis of 'torsional oscillations' in Earth's core [Gillet et al., 2010].

It is also observed that the Lowes-Mauersberger spectrum of magnetic energy is flat at the core-mantle boundary up to harmonic degree 13 [e.g., Langlais et al., 2014]. This means that energy is independent of length scale in this scale-range, which translates into a  $\tau_b(\ell) \propto \ell$  trend at large-scale (see Appendix A.2.1). Similarly, core flow inversions favor an almost flat harmonic spectrum of kinetic energy up to degree 13 [Aubert, 2013, Gillet et al., 2015, Baerenzung et al., 2016]. These trends are sketched in Figure 2.

## 4. $\tau$ - $\ell$ regime diagrams for non-magnetic rotating core

We first present a reference model of rapidly rotating convection in a sphere, which we illustrate with the  $\tau$ - $\ell$  diagram of an actual numerical simulation. We then propose an idealized scenario of turbulent convection in Earth's core in the absence of a magnetic field.

### 4.1. turbulence regimes for rotating convection

Many different turbulence regimes can occur in rotating convection, depending upon which forces are dominant in Navier-Stokes equation (see Gillet and Jones [2006], Julien et al. [2012], Gastine et al. [2016], Guzmán et al. [2021] for reviews). In Appendix B, we present the main relevant force balances for planetary cores, and their  $\tau$ - $\ell$  translation.

We focus here on rapid rotation regimes, for which leading order balance is quasi-geostrophic (small Rossby number), implying that convection is organized in columnar vortices aligned with planet's spin axis. Next order balance controls turbulence in planes perpendicular to the spin axis. In the absence of a magnetic field, the relevant balance is between vortex advection, vortex stretching and vortex generation by buoyancy, the so-called QG-CIA balance (see Jones [2015], Schwaiger [2020]).

Introducing scales  $\ell_{\parallel} \sim R_o$  the height of convective columns, and  $\ell_{\perp}$  their radius in QG-CIA equilibrium, we get (see Appendix B.3):

$$t_{\Omega} \tau_u(\ell_{\parallel}) \sim \tau_p^2(\ell_{\perp}) \sim \tau_u^2(\ell_{\perp}). \quad (15)$$

Further assuming  $\tau_u(\ell) \propto \ell$  between  $\ell_{\perp}$  and  $R_o$ , one obtains:

$$\ell_{\perp} \sim R_o \frac{t_{\Omega}}{\tau_u(\ell_{\perp})} = \sqrt{\frac{u(\ell_{\perp}) R_o}{\Omega}}, \quad (16)$$

which means that the system is in a Rhines state at  $\ell_{\perp}$ , and thus that  $\tau_u(\ell_{\perp})$  lies on Rossby line.

This scenario is well supported by the study of Guervilly et al. [2019], who performed numerical simulations of thermal convection at low Prandtl number in a sphere, at Ekman numbers down to  $\text{Ek}(R_o) = 10^{-8}$  in 3D and to  $\text{Ek}(R_o) = 10^{-11}$  in quasi-geostrophic 2D.

They find that dominant convective scale  $\ell_{\perp}$  obeys a QG-CIA balance, and they derive simple scaling laws, which translated in  $\tau$ - $\ell$  terms (assuming their  $U_{rms} \simeq u(\ell_{\perp})$ ) yield:

$$\ell_{\perp} / R_o = 8.5 \text{Ro}_{ff}(R_o) \quad (17)$$

and:

$$\text{Ro}(\ell_{\perp}) = 0.6 \frac{R_o}{\ell_{\perp}} (\text{Ro}_{ff}(R_o))^2, \quad (18)$$

where  $\text{Ro}(\ell)$  and  $\text{Ro}_{ff}(\ell)$ , are  $\ell$ -scale Rossby and free-fall Rossby numbers, respectively, as defined in Table III. Combining equations (17) and (18), and dropping prefactors, one recovers equation (16).

Figure 3a displays the  $\tau$ - $\ell$  diagram of Guervilly et al. [2019]'s most extreme 3D simulation. We use radius  $R_o$  and  $t_{\Omega}$  (rotation rate's inverse) of the actual Earth core as length-scale and timescale, respectively, from which we draw lines  $t_{\Omega}$  and  $\tau_{Rossby}$ . Input dimensionless parameters of the simulation ( $\text{Ek}(R_o) = 10^{-8}$ ,  $\text{Pr} = 10^{-2}$ ) provide values needed to build lines  $\tau_v$  and  $\tau_{\kappa}$ . Gravity is obtained from Rayleigh number  $\text{Ra}(R_o) = 2.5 \times 10^{10}$ . Power dissipation markers are drawn, using outer core mass  $M_o$ .

Volumetric averages of azimuthal order  $m$ -spectra of a snapshot of this simulation are converted in  $\tau_u(\ell)$  and  $\tau_{\rho}(\ell)$  lines, following equations (42) and (44) of Appendix A.2.2. Flow becomes anisotropic at large length-scale, as shown by the additional  $\tau_{u_r}(\ell)$  line of radial velocities. This line displays a sharp timescale minimum, defining length-scale  $\ell_{\perp}$ , which coincides with the length-scale given by power dissipation occurring in Ekman layers (horizontal dashed line pinned to the Rossby line), which is slightly larger than bulk viscous dissipation (marked by a dashed line attached to line  $\tau_v(\ell)$ ). QG-CIA balance seems satisfied within one order of magnitude with  $\tau_{Rossby}(\ell_{\perp}) \sim \tau_u(\ell_{\perp}) \sim \tau_{\rho}(\ell_{\perp})$ . Note that line  $\tau_u(\ell)$  stays above Rossby line at all length-scales, in line with the high degree of  $z$ -invariance observed in this simulation.

#### 4.2. $\tau$ - $\ell$ diagram for a non-magnetic Earth core

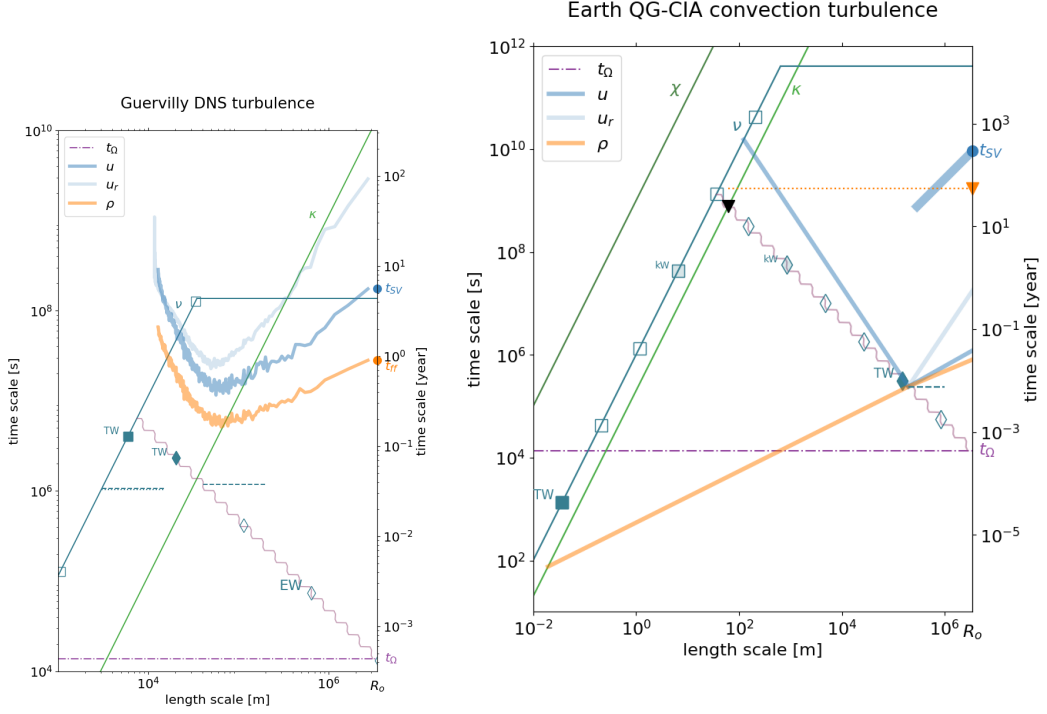
We now have all elements to start building a  $\tau$ - $\ell$  scenario for rotating convection in a non-magnetic Earth's core, which we present in Figure 3b. Adopting a QG-CIA balance, we further require that viscous dissipation mainly occurs in Ekman layers, at the 'optimum' radius of convective columns  $\ell_{\perp} = \ell_*$ , which lies on the Rossby line. From power dissipation markers along the Rossby line, we place the optimum at time  $\tau_* = \left[ \frac{M_o R_o}{\mathcal{P}_{diss}} \sqrt{\frac{v}{\Omega^3}} \right]^{1/4}$ , which provides requested  $\mathcal{P}_{diss}$ .

While the second term of QG-CIA balance in equation (58) predicts  $\tau_{\rho}(\ell_{\perp}) = \tau_u(\ell_{\perp})$ , Guervilly et al. [2019]'s results indicate  $\tau_{\rho}(R_o) = \tau_u(\ell_{\perp})$ . Rather arbitrarily, we stick to QG-CIA balance and assume that density anomalies do not depend on length-scale, which translates into  $\tau_{\rho}(\ell) \propto \ell^{1/2}$ .

It remains to draw line  $\tau_u(\ell)$  for  $\ell$  smaller and larger than  $\ell_{\perp}$ . Figure 3 of Guervilly et al. [2019] shows that kinetic energy cascades steeply to small scales below  $\ell_{\perp}$  scale, with a spectrum  $E(m) \propto m^{-5}$ , where  $m$  is the azimuthal wavenumber, which we translated into  $\tau_u(\ell) \propto \ell^{-3/2}$  following equation (42) of Appendix A.2.2<sup>1</sup>. Flow becomes anisotropic for  $\ell > \ell_{\perp}$ , with radial velocities decreasing as  $\ell$  increases, while azimuthal velocities increase with  $\ell$ . We loosely prescribe  $\tau_{u_r}(\ell) \propto \ell^{3/2}$  and  $\tau_{u_{az}}(\ell) \simeq \tau_u(\ell) \propto \ell^{1/2}$  for  $\ell > \ell_{\perp}$ .

Reading the  $\tau$ - $\ell$  diagram of Figure 3b, we see that core flow in a non-magnetic Earth would be quasi-geostrophic at all scales, with azimuthal velocities reaching 3 m s<sup>-1</sup>, much larger than present-day core flow velocities represented by its  $t_{SV}$  value and trend. The radius of dominant columnar vortices would be around 200 km. Ekman layer viscous dissipation would dominate over bulk viscous dissipation by many orders of magnitude.

<sup>1</sup>Note that  $\tau_u(\ell)$  scales as  $\ell^{-1}$  and plots along the Rossby line if we use equation (33) instead, as in Rhines [1975].



(a) 3D simulation from Guervilly et al. [2019].

(b) QG-CIA scenario for a non-magnetic Earth core.

**Figure 3.**  $\tau$ - $\ell$  diagrams for non-magnetic rapidly rotating convection. Same conventions as in Figures 1 and 2. The thick orange line is  $\tau_\rho(\ell)$ . Radial flow velocities  $u_r$  (pale blue) are smaller than azimuthal velocities at large length scales. (a) 3D numerical simulation from Guervilly et al. [2019] scaled to Earth parameters. Blue horizontal dashed lines mark viscous dissipation in the bulk (pinned to line  $\tau_v(\ell)$ ) and in Ekman layers (pinned to Rossby line). (b) Scenario for the Earth assuming a QG-CIA force balance. The dominant vortex radius at  $\ell = \ell_\perp = \ell_*$  is pinned to dissipation time  $\tau_*$  (blue dashed line) on the Rossby line. Line  $\tau_u(\ell)$  splits in two lines for  $\ell > \ell_\perp$ , with stronger azimuthal velocities than radial velocities (label  $u_r$ ). Flow and density time- and length-scales at convection threshold are marked by black and orange triangles, respectively (see text).

We observe that relations between  $\ell_\perp$ ,  $\tau_u(\ell_\perp)$  and  $\tau_\rho(\ell_\perp)$  resemble those between  $\ell_c$ ,  $\tau_c$  and  $\tau_{\rho_c}$ , where  $\ell_c$  is the critical wavelength of convective instability at convection onset,  $\tau_c$  the corresponding period, and  $\tau_{\rho_c}$  the critical density threshold, as defined in Supplementary Material 's section S1. In Figure 3b, we plot  $(\ell_c, \tau_c)$  and  $(R_o, \tau_{\rho_c})$  as black and orange triangles, respectively. Starting from  $(\ell_c, \tau_c)$ , convective optimum 'slides' along Rossby line as more power is given to the system, towards larger Ekman layer dissipation, which gradually dominates over bulk viscous dissipation.

## 5. $\tau$ - $\ell$ regime diagrams for Earth's core

In this section, we examine which  $\tau$ - $\ell$  regime diagrams to expect for the Earth's core. Our goal is not to come up with an optimal or accurate scenario, but rather to illustrate how  $\tau$ - $\ell$  diagrams can help inventing and testing

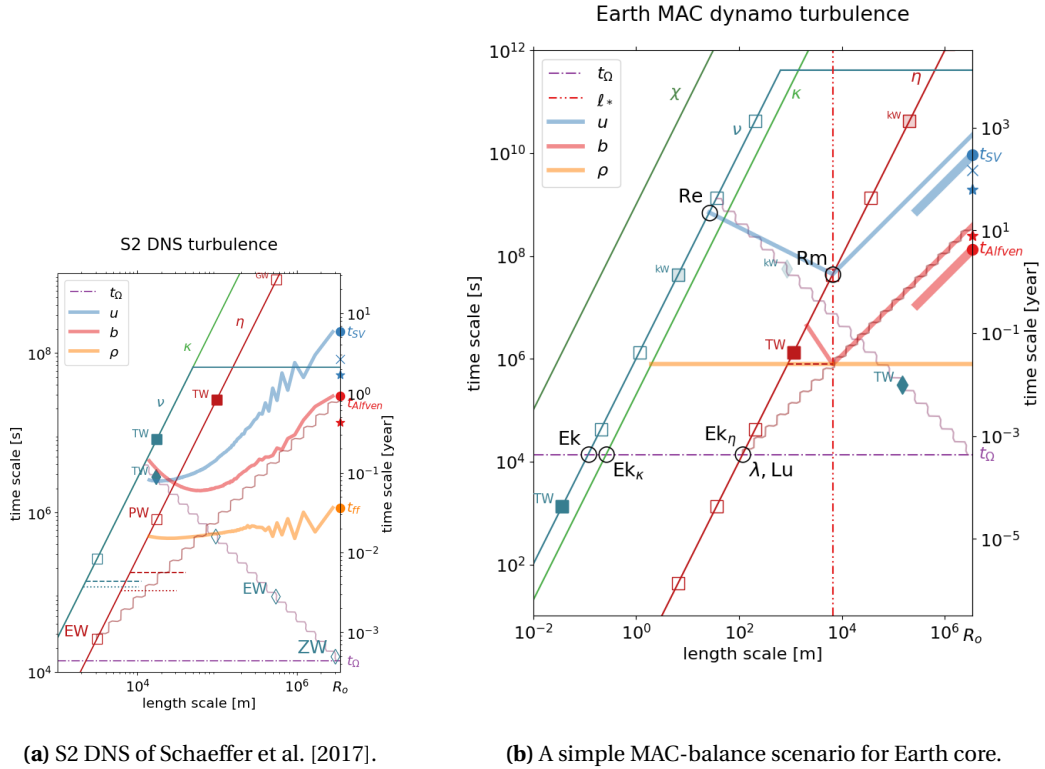


**Figure 4.**  $\tau$ - $\ell$  diagrams for rapidly rotating convective dynamo. Same conventions as in Figure 2. Blue, red and orange lines are  $\tau_u(\ell)$ ,  $\tau_b(\ell)$  and  $\tau_\rho(\ell)$ , respectively. Red and blue stars on the right  $y$ -axis mark magnetic intensity and velocity amplitude, respectively, predicted by Christensen and Aubert [2006]’s scaling laws. Blue cross from Davidson [2013]’s velocity scaling law. (a) 3D numerical simulation S2 of Schaeffer et al. [2017], scaled to Earth parameters. Red and blue horizontal dashed lines mark ohmic and viscous dissipation, respectively, as measured in the simulation. Dotted lines indicate approximated values discussed in Appendix A.3. (b) Scenario for the Earth assuming a MAC force balance. Ohmic dissipation of available convective power  $\mathcal{P}_{diss}$  is marked by a blue horizontal dashed line pinned to line  $\tau_\eta(\ell)$ . It controls length scale  $\ell_*$  (indicated by a red vertical dash-dot line) at which turbulence regime changes. Circles labeled Re and Rm at the intersections of line  $\tau_u$  with lines  $\tau_v(\ell)$  and  $\tau_\eta(\ell)$  mark the scales at which the corresponding  $\ell$ -scale dimensionless number (see Table III) equals 1.

such scenarios. We now consider the presence of a magnetic field and try to document Earth’s core  $\tau$ - $\ell$  diagram, for which we presented a template in Figure 2.

Let us start by building and discussing the  $\tau$ - $\ell$  regime diagram (Figure 4a) of one of the most extreme dynamo simulation available today: the S2 DNS of Schaeffer et al. [2017]. We use radius  $R_o$  and  $t_\Omega$  of the actual Earth core as length-scale and timescale, respectively, from which we draw lines  $t_\Omega$  and  $\tau_{Rossby}(\ell)$ . Input dimensionless parameters of the simulation ( $Ek(R_o - R_i) = 10^{-7}$ ,  $Pr = 1$ ,  $Pm = 0.1$ ) provide values needed to build lines  $\tau_v(\ell)$ ,  $\tau_\kappa(\ell)$  and  $\tau_\eta(\ell)$ . Power dissipation markers are drawn, using outer core mass  $M_\rho$ .

Lines  $\tau_u(\ell)$  and  $\tau_b(\ell)$  are the  $\tau$ - $\ell$  translation of the magnetic and velocity energy  $n$ -degree spectra (time-averaged volumetric average), as obtained by applying equations (42) and (43) of Appendix A.2.3, respectively, replacing  $R_o$  by the volumetric average of radius ( $0.77 R_o$ ).  $t_{SV}$  and  $t_{Alfven}$  are deduced from their largest

scale values (spherical harmonic degree  $n = 1$ ). The simulated acceleration of gravity  $g$  at the top boundary is obtained from:

$$g = \frac{\text{Ra}^* R_o \kappa \nu}{(R_o - R_i)^4}, \quad (19)$$

with  $\text{Ra}^* = \text{Ra}/\beta R_o = 2.4 \times 10^{13}$ , where  $\text{Ra}$  is the classical large-scale Rayleigh number, and  $\beta$  the imposed codensity gradient at the top boundary. We then obtain line  $\tau_\rho(\ell)$  by applying equation (44) to the codensity spectrum multiplied by  $\text{Pr}^2$ . Ohmic and viscous dissipations  $D_\eta$  and  $D_\nu$  of Table 2 of Schaeffer et al. [2017] are scaled to Earth's core by:  $\mathcal{P} = D\rho\nu^3/(R_o - R_i)$ , and are shown as horizontal dashed lines attached to lines  $\tau_\eta(\ell)$  and  $\tau_\nu(\ell)$ , respectively (see Appendix A.3 for discussion).

Reading the resulting  $\tau$ - $\ell$  diagram, we see that: magnetic energy largely dominates over kinetic energy ( $t_{Alfven} \ll t_{SV}$ ); Ohmic dissipation dominates over viscous dissipation (compare dissipation powers indicated by horizontal dashed lines pinned to lines  $\tau_\eta(\ell)$  and  $\tau_\nu(\ell)$ , respectively); flow should be largely quasi-geostrophic, since the  $\tau_u(\ell)$  line stays above the Rossby line down to dissipation length-scales. We also observe that both lines  $\tau_u(\ell)$  and  $\tau_b(\ell)$  have slopes close to 1 at large length-scale, while  $\tau_\rho(\ell)$  line is nearly horizontal, and that the intersection of lines  $\tau_\eta(\ell)$  and  $t_{Alfven}$  is close to that of lines  $\tau_\eta(\ell)$  and  $t_\Omega$ .

We now examine different scenarios for Earth's core, testing several of the force balances defined in Appendix B.

### 5.1. A simple MAC-balance scenario

Figure 4b proposes a first attempt to document the template of Figure 2. Because magnetic diffusivity is much larger than viscosity, dissipation in the core is expected to be mostly Ohmic. We formulate the ansatz that available convective power  $\mathcal{P}_{diss}$  is dissipated by Joule heating, which means that  $\tau_b(\ell)$  line should get down to (but not below) time  $\tau_* = \sqrt{M_o\eta/\mathcal{P}_{diss}}$  that yields a dissipation equal to  $\mathcal{P}_{diss}$ . This time is drawn as a horizontal dashed line pinned to line  $\tau_\eta(\ell)$  in Figure 4b.

We now need to guess at which  $\ell = \ell_*$  the  $\tau_b$  line should hit that line. For a maximum Ohmic dissipation to be obtained at that level,  $\tau_b$  line should rise up for  $\ell < \ell_*$ . We infer that this change should be caused by a flow modification. Once  $\tau_u$  line crosses  $\tau_\eta$  line, flow enters a regime of low  $\text{Rm}$  magnetohydrodynamic (MHD) turbulence in presence of a strong magnetic field, in which the intensity of the induced magnetic field  $b$  is severely reduced. This suggests  $\text{Rm}(\ell_*) \sim 1$ , which implies:

$$\text{Rm}(\ell_*) = \frac{\tau_\eta(\ell_*)}{\tau_u(\ell_*)} = 1. \quad (20)$$

This first condition links velocity field to magnetic field but is not sufficient to provide  $\ell_*$ . We need another hypothesis. In this simple scenario, we assume that the system achieves a MAC force balance (see Appendix B.4) at dissipation scale  $\ell_*$ .

We deduce that  $\ell$ -scale Elsasser number is also equal to 1 at  $\ell = \ell_*$ .

$$\Lambda(\ell_*) = \frac{\tau_u(\ell_*) t_\Omega}{\tau_b(\ell_*) \tau_{Alfven}(\ell_*)} = 1. \quad (21)$$

Further assuming  $\tau_b(\ell_*) = \tau_{Alfven}(\ell_*)$ , meaning that  $\ell_*$  lies on the Alfvén line, we combine equations (20) and (21) and obtain:

$$\tau_* \equiv \tau_b(\ell_*) = \sqrt{t_\Omega \tau_\eta(\ell_*)}. \quad (22)$$

Graphically, this means that  $\ell_*$  is such that distance between  $\tau_\eta(\ell_*)$  and  $\tau_*$  equals distance between  $\tau_*$  and  $t_\Omega$ .

Length-scale  $\ell_*$  is obtained by:

$$\left(\frac{\ell_*}{R_o}\right)^2 = \frac{\tau_* \tau_*}{t_\Omega T_\eta} = \frac{1}{t_\Omega T_\eta^2} \frac{M_o R_o^2}{\mathcal{P}_{diss}}, \quad (23)$$

where  $T_\eta = \tau_\eta(R_o)$ . MAC balance also provides  $\tau_\rho(\ell_*) = \tau_b(\ell_*) = \tau_*$ . Assuming that  $\tau_\rho(\ell)$  does not depend upon  $\ell$  provides the orange horizontal line in Figure 4b.



The regime of MHD turbulence in the presence of a strong magnetic field for  $\ell < \ell_*$  is characterized by steep energy spectra:  $E(k) \propto k^{-3}$  and  $E_m(k) \propto k^{-5}$  [Alemany et al., 1979], yielding the slopes drawn for  $\tau_u(\ell)$  and  $\tau_b(\ell)$ , respectively, in Figure 4b (see Appendix A.1). Adding rotation further reduces turbulence level [Nataf and Gagnière, 2008, Kaplan et al., 2018], but we lack constraints on the resulting energy spectra (but see Supplementary Material's section S3).

In the dynamo region ( $\ell > \ell_*$ ), we assume a  $k^{-1}$  energy density spectrum (*i.e.*,  $\tau(\ell) \propto \ell$ ). This is consistent with our assumption that point  $(\ell_*, \tau_*)$  lies on the Alfvén line, and is also suggested by Figure 4a and observations, as discussed in section 3.3. But the main motivation is pedagogical, as explained below.

At the largest scale, our scenario yields velocity and magnetic amplitudes that are not too far from the observed  $t_{SV}$  and  $t_{Alfven}$  values. They translate into a magnetic to kinetic energy ratio of about  $10^4$ , according to equations (6) and (14). Bulk and boundary viscous dissipations have comparable amplitudes, both several orders of magnitude smaller than Ohmic dissipation, as assumed.

The smallest QG vortices are very sluggish, with a turnover time of about 1 year and a radius of 1 km. Magnetic diffusion is largest at a length-scale of about 10 km.

It is interesting to observe that our scenario implies that Alfvén line intersects  $\tau_\eta$  line at  $t_\Omega$ , meaning that all three  $\ell$ -scale dimensionless numbers  $Ek_\eta$ ,  $Lu$  and  $\lambda$  equal 1 at this same scale. This implies that  $B_0$  can be deduced from the intersection of lines  $\tau_\eta$  and  $t_\Omega$ . In other words, even though our scenario has been built to achieve a given Ohmic dissipation  $\mathcal{P}_{diss}$ , the actual value of  $B_0$  does not depend on  $\mathcal{P}_{diss}$ . Only the kinetic energy depends on  $\mathcal{P}_{diss}$ .

## 5.2. A simple QG-MAC balance scenario

In our simple MAC-balance scenario, all length-scales  $\ell > \ell_*$  have  $\Lambda(\ell) < 1$ , while  $\tau_u(\ell)$  velocity line remains above Rossby line in the dynamo generation domain ( $Rm(\ell) > 1$ ). Leading-order force balance should therefore be quasi-geostrophic, with convective motions forming columnar vortices parallel to the rotation axis, and we should rather target a QG-MAC force balance to build our  $\tau_u$ ,  $\tau_b$  and  $\tau_\rho$  lines.

Appendix B.5 recalls that QG-MAC balance for columns of radius  $\ell_\perp$  and length  $\ell_\parallel \sim R_o$  writes:

$$\frac{\Omega u}{\ell_\parallel} \sim \frac{b^2}{\rho \mu \ell_\perp^2} \sim \frac{\Delta \rho}{\rho} \frac{g}{\ell_\perp}, \quad (24)$$

which translates into:

$$t_\Omega \tau_u(\ell_\parallel) \sim \tau_b^2(\ell_\perp) \sim \tau_\rho^2(\ell_\perp), \quad (25)$$

One then needs to guess at which scale  $\ell_\perp$  this balance should apply. One cannot choose  $\ell_\perp = \ell_*$  as in our simple MAC scenario, because this would place  $\tau_u(\ell_*)$  very far down, below the  $t_\Omega$  line, breaking quasi-geostrophy, and yielding  $\mathcal{E} \gg \mathcal{E}_m$  in strong disagreement with observations.

Figure 5a displays the  $\tau$ - $\ell$  diagram of a QG-MAC scenario with  $\ell_\perp = R_o/10$ . We retain the same hypotheses as in our MAC scenario:  $\tau_u(\ell) \propto \ell$  and  $\tau_b(\ell) \propto \ell$  for  $\ell_* < \ell < R_o$ , together with  $Rm(\ell_*) = 1$  and  $\tau_b(\ell_*) = \tau_*$  fixed by  $\mathcal{P}_{diss}$ .

QG-MAC balance at scale  $\ell_\perp$  then yields:

$$\left(\frac{\ell_*}{R_o}\right)^3 = \left(\frac{\ell_\perp}{R_o}\right)^2 \frac{\tau_*}{t_\Omega} \frac{\tau_*}{T_\eta}. \quad (26)$$

Comparing with Figure 4b, we see that this scenario predicts a larger magnetic over kinetic energy ratio, with  $\tau_u$  above the Rossby line down to scales of a few hundred meters. Another difference is the level of line  $\tau_\rho(\ell)$ , now at time  $\tau_b(\ell_\perp)$  instead of  $\tau_*$  in our MAC scenario.

## 5.3. A QG-MAC balance scenario à la Aubert

In previous scenario, choosing  $\ell_\perp = R_o/10$  was borrowed from Aubert et al. [2017] and Aubert [2019], who find it in good agreement with numerical simulation results. Following Davidson [2013], Aubert [2019] proposes a

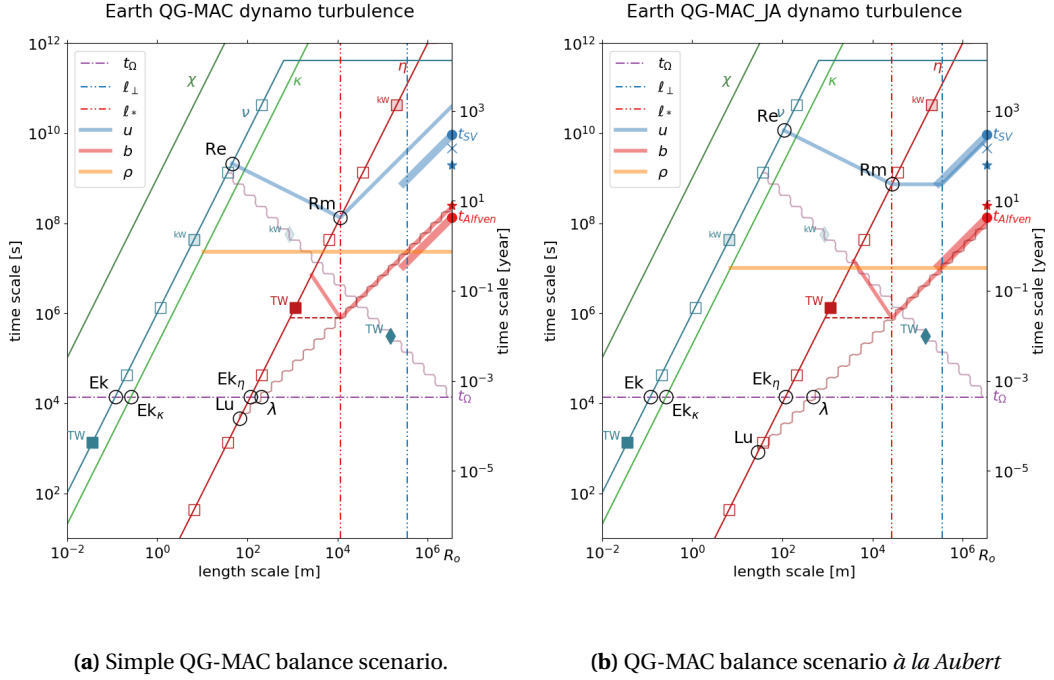


**Figure 5.**  $\tau$ - $\ell$  regime diagrams of two QG-MAC balance scenarios, which only differ by the  $\tau_u(\ell)$  scaling law chosen for  $\ell_* < \ell < \ell_\perp$ . Blue vertical dash-dot line indicates length scale  $\ell_\perp$ . See figure 4b for other indications.

$\tau_u(\ell)$  scaling for  $\ell_* < \ell < \ell_\perp$  that differs from the one we used in section 5.2. In that interval, Davidson [2013] infers that vorticity, rather than velocity, is independent of  $\ell$ . This translates into  $\tau_u(\ell)$  being constant instead of  $\tau_u(\ell) \propto \ell$ .

Keeping our other hypotheses,  $\ell_*$  is then given by:

$$\left(\frac{\ell_*}{R_o}\right)^4 = \left(\frac{\ell_\perp}{R_o}\right)^3 \frac{\tau_*}{t_\Omega T_\eta}. \quad (27)$$

The corresponding  $\tau$ - $\ell$  regime diagram is shown in Figure 5b. It agrees amazingly well with observed  $t_{SV}$  and  $t_{Alfven}$  values and trends. The  $\tau_u(\ell)$  line is even higher above Rossby line than in previous scenario. However, keeping in mind the criterion that defines MAC-balance ( $\tau_b$  at mid-distance between  $t_\Omega$  and  $\tau_u$  from equation (60) in Appendix B.4), we observe that magnetic field might damage quasi-geostrophy at a length-scale  $\ell_{MAC}$  not far below  $\ell_\perp$ . In fact, we get:

$$\frac{\ell_{MAC}}{R_o} = \left(\frac{\ell_\perp}{R_o}\right)^{3/2} \simeq \frac{1}{32}. \quad (28)$$

#### 5.4. The interesting case of Venus

The internal structure of Venus is very poorly known, but we know that it does not generate a magnetic field. This important difference from its sister planet Earth is classically explained by a different thermal history, leading to a hot mantle convecting beneath a rigid lid, preventing core cooling, hence halting the convective engine of the dynamo [Stevenson et al., 1983, Nimmo, 2002].

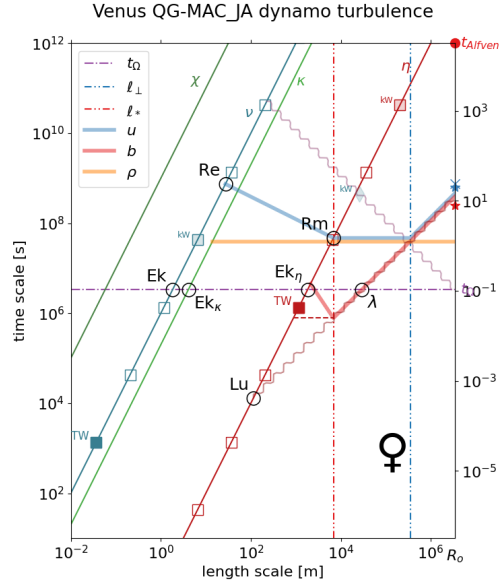


**Figure 6.** Devil’s advocate  $\tau$ - $\ell$  regime diagram for Venus, copied from scenario QG-MAC *a la Aubert* of Figure 5b, assuming Earth’s core parameters, except for spin rate taken as the actual one of Venus (rotation period of 243 days). This diagram predicts a magnetic intensity comparable to that of the Earth, incompatible with the observed upper bound shown by  $t_{Alfven}$  at the top of right  $y$ -axis. It serves as an illustration of regime changes due to spin rate.

Venus and Earth also differ by their spinning rate: one turn in 243 days instead of one day. This difference is usually considered as unimportant since rotation still appears overwhelming, with an Ekman number  $Ek(R_o) \sim 10^{-13}$  [Russell, 1980].

However, if we adopt for Venus the same physical properties as for Earth, including its available convective power  $\mathcal{P}_{diss}$ , but update the spinning rate to the one of Venus, we encounter a problem, illustrated in Figure 6.

While pulling Earth’s core out of the validity region of a QG-MAC regime seems to require very unrealistic values of convective power, as we discuss in next section, the TW dissipation mark falls below the  $t_\Omega$  line of Venus, for both Ohmic dissipation and Ekman friction (for which the marker falls beyond  $\ell = R_o$  axis on Rossby line).

Applying the same QG-MAC scenario as in section 5.3 places the dynamo-generating region well within the non-quasigeostrophic triangle, defeating the assumed force balance. A difference subsists in the absence of a magnetic field: we cannot apply the QG-CIA balance of section 4.1 since  $\mathcal{P}_{diss}$  cannot be dissipated by Ekman friction alone.

Our exercise is very formal since we recall that there are good reasons to believe that such a  $\mathcal{P}_{diss}$  is not available for Venus [Stevenson et al., 1983, Nimmo, 2002]. Nevertheless, our diversion to Venus questions the notion of ‘rapid rotator’ and shows that for a given convective power  $\mathcal{P}_{diss}$ , planet’s spin rate might play a more important role than simply inferred from the low Ekman number it delivers. MAC balance of section 5.1 suggests that a rough condition for rapid rotator dynamo is  $\mathcal{P}_{diss} < \Omega^2 \eta M_o$ .

## 6. Discussion

We discuss here what can be read from the  $\tau$ - $\ell$  diagrams we presented, and how they relate to previous work.

### 6.1. Scenario validity domain

One goal of our approach is to better appreciate the validity domain of the various regimes encountered in planetary cores. For example, no dynamo will exist if line  $\tau_u(\ell)$  plots too high in the diagram, yielding  $\text{Rm}(R_o) \sim 1$ . In Earth's core, this would only happen for  $\mathcal{P}_{diss}$  values several orders of magnitude smaller than our reference value of 3 TW. Actually, very low values (even negative) are not excluded by some thermal history models, before the birth of the inner core (e.g., Landeau et al. [2022]). At the other end, large  $\mathcal{P}_{diss}$  values can pull the dynamo generation domain ( $\text{Rm}(\ell) > 1$ ) partly beneath the Rossby line. Complete columnar vortices won't then have time to form at length-scales below the Rossby line, and we might have a somewhat different turbulence regime. Davidson [2014] proposed an original dynamo scenario that corresponds to such a situation. Noting that inertial waves are strongly helical, and that flow helicity is a key ingredient for dynamo action, he suggests that Earth's dynamo might operate this way. None of the three scenarios we presented (Figures 4b, 5a, 5b) puts  $\text{Rm} \sim 1$  below the Rossby line. However, it would only take  $\mathcal{P}_{diss} \simeq 12$  TW for the MAC scenario (Figure 4b) to qualify (remember we only consider orders of magnitude).

Also note that in all three scenarios, dynamo gets closer to equipartition ( $\tau_u(\ell) = \tau_b(\ell)$ ) as  $\mathcal{P}_{diss}$  increases.

While Earth's core turbulence regime seems relatively immune to convective power variations, Venus' devil's advocate (Figure 6) indicates that a lower spin rate can have a strong effect. We think that  $\tau$ - $\ell$  diagrams should be drawn for planets and stars before inferring their dynamo characteristics.

### 6.2. Dynamo scaling laws

Christensen [2010] nicely reviews a number of scaling laws proposed to infer the magnetic field intensity of planets (and stars). Among the nine proposed scaling laws he lists, five relate magnetic intensity to planetary rotation rate  $\Omega$ , with no influence of the available convective power  $\mathcal{P}_{diss}$ , three involve both  $\Omega$  and  $\mathcal{P}_{diss}$ , and one only  $\mathcal{P}_{diss}$ . The latter one, first proposed by Christensen and Aubert [2006], stems from the analysis of a large corpus of numerical simulations of the geodynamo, backed by an appraisal of the dominant terms in the governing equations. It is the law preferred by Christensen [2010] who shows that it is in good agreement with the measured magnetic intensity of planets and stars.

Translated in  $\tau$ - $\ell$  formulation, Christensen's preferred laws yield:

$$\tau_u(R_o) = \frac{1}{c_u} \left( \frac{M_o R_o^2 \Omega^{1/2}}{\bar{F} \mathcal{P}_{diss}} \right)^{2/5} \simeq \left( \frac{T_\eta^2 \tau_*^4}{t_\Omega} \right)^{1/5} \quad (29)$$

$$\tau_b(R_o) = \frac{1}{\sqrt{2c_b f_{ohm}}} \left( \frac{M_o R_o^2}{\bar{F} \mathcal{P}_{diss}} \right)^{1/3} \simeq (T_\eta \tau_*^2)^{1/3}, \quad (30)$$

from equations (32) and (15) of Christensen [2010], assuming that energies are in this largest-scale component, with  $\bar{F} = F/3.1$ , and converting  $\mathcal{P}_{diss} = 4\pi R_o^2 q_o$ , with  $q_o$ ,  $f_{ohm}$ ,  $c_u \simeq 1.05$ ,  $c_b \simeq 0.63$ , and  $F \simeq 1$  as he defines them. Both large-scale flow velocity  $U$  and magnetic field  $B$  do not depend upon magnetic diffusivity<sup>2</sup>, and  $B$  is also independent of spin rate  $\Omega$ . These predictions are displayed by blue and red stars on the right axis in Figures 4, 5, and 6. While  $B$ -prediction agrees well with observations,  $U$ -prediction over-estimates flow velocity.

<sup>2</sup>Note that one can define a dissipation time  $T_{diss} = \sqrt[3]{\frac{M_o R_o^2}{\mathcal{P}_{diss}}}$ , which makes it more explicit that  $T_\eta \tau_*^2 = T_{diss}^3$  is independent of magnetic diffusivity  $\eta$ .

Davidson [2013] re-examined this question and noted that inertia is playing too strong a role in Christensen and Aubert [2006]’s simulations. He derived a MAC-balance variant and obtained a revised flow velocity law (his equation (15)), which translates into:

$$\tau_u(R_o) \simeq \Omega^{1/3} \left( \frac{M_o R_o^2}{\mathcal{P}_{diss}} \right)^{4/9} = \left( \frac{T_\eta^4 \tau_*^8}{t_\Omega^3} \right)^{1/9}, \quad (31)$$

in which  $U$  is independent of magnetic diffusivity  $\eta$ . Davidson’s prediction is drawn as a blue  $\times$  in Figures 4, 5, and 6.

Our discussion on scenario validity domain questions the obtention of universal dynamo scaling laws. However, such scaling laws can be easily derived for the three scenarios we presented, and they nicely illustrate the diversity one can get. Each scenario produces  $\tau_u(R_o)$  and  $\tau_b(R_o)$  that combine  $\tau_*$  (or  $T_{diss}$ ),  $T_\eta$  and  $t_\Omega$  with various powers.

Our MAC scenario produces:

$$\begin{aligned} \tau_u(R_o) &= \left( \frac{T_\eta \tau_*^2}{t_\Omega} \right)^{1/2} = \left( \frac{\Omega M_o R_o^2}{\mathcal{P}_{diss}} \right)^{1/2} \\ \tau_b(R_o) &= (t_\Omega T_\eta)^{1/2} = \frac{R_o}{\sqrt{\Omega \eta}}, \end{aligned}$$

for which  $B$  is independent of  $\mathcal{P}_{diss}$ , and  $U$  is independent of magnetic diffusivity  $\eta$ .

The QG-MAC scenario yields:

$$\begin{aligned} \tau_u(R_o) &= \left( \frac{\ell_\perp}{R_o} \right)^{2/3} \left( \frac{T_\eta^2 \tau_*^2}{t_\Omega} \right)^{1/3} = \left( \frac{\ell_\perp}{R_o} \right)^{2/3} \left( \frac{\Omega R_o^2 M_o R_o^2}{\eta \mathcal{P}_{diss}} \right)^{1/3} \\ \tau_b(R_o) &= \left( \frac{R_o}{\ell_\perp} \right)^{2/3} (t_\Omega T_\eta \tau_*)^{1/3} = \left( \frac{R_o}{\ell_\perp} \right)^{2/3} \left( \frac{\eta M_o R_o^2}{\Omega^4 R_o^2 \mathcal{P}_{diss}} \right)^{1/6} \end{aligned}$$

And our QG-MAC *a la Aubert* scenario gives:

$$\begin{aligned} \tau_u(R_o) &= \left( \frac{\ell_\perp}{R_o} \right)^{1/2} \left( \frac{T_\eta \tau_*^2}{t_\Omega} \right)^{1/2} = \left( \frac{\ell_\perp}{R_o} \right)^{1/2} \left( \frac{\Omega M_o R_o^2}{\mathcal{P}_{diss}} \right)^{1/2} \\ \tau_b(R_o) &= \left( \frac{R_o}{\ell_\perp} \right)^{3/4} (t_\Omega T_\eta \tau_*^2)^{1/4} = \left( \frac{R_o}{\ell_\perp} \right)^{3/4} \left( \frac{M_o R_o^2}{\Omega \mathcal{P}_{diss}} \right)^{1/4}, \end{aligned}$$

predicting  $U$  and  $B$  independent of magnetic diffusivity  $\eta$ , unless  $\ell_\perp/R_o$  depends upon  $\eta$ .

### 6.3. Strong and weak dynamos

All three MAC-type scenarios we presented produce a magnetic field whose energy is several orders of magnitude larger than kinetic energy, as observed for the Earth. They thus belong to the category of ‘strong-field’ dynamos. Dormy [2016] points out that strong-field dynamos can be obtained in numerical simulations with large magnetic Prandtl number  $Pm = \nu/\eta$ . He stresses that minimising  $Pm$  at a given Ekman number  $Ek(R_o) = \nu/\Omega R_o^2$  is not a good strategy to approach Earth core regimes, since it increases magnetic Ekman number  $Ek_\eta(R_o) = \eta/\Omega R_o^2$ . Similarly, Christensen et al. [2010] show that  $Ek_\eta(R_o) < 10^{-4}$  is needed for obtaining Earth-like geodynamo models. In all scenarios we explored, viscosity  $\nu$  plays no role, while magnetic Ekman has a crucial role (see section 5.4 in particular).

Our three MAC-type scenarios can easily be built with large  $Pm$ , while retaining all characteristics of Earth-like dynamos:  $\mathcal{E}_m \gg \mathcal{E}$ , dominant Ohmic dissipation, and MAC force balance. However, we find that the examples produced by Dormy [2016] depart from these conditions, because viscosity strongly controls their patterns, as shown in Supplementary Material’s section S2.

## 7. Limitations and perspectives

Let us first recall that our  $\tau$ - $\ell$  approach is *not* a theory of turbulence. We try to formulate plausible scenarios by identifying scales at which a change in turbulence regime should occur, and by patching scaling laws appropriate for each regime. We thus entirely depend on the availability of such laws, which can be brought by experiments, theory, and numerical simulations.

For simplicity reasons, we have treated planetary cores as simple full spheres. The application to actual planets requires to at least consider spherical shells of various thicknesses instead. An extension to giant planets and stars also requires taking into account compressibility and free-slip boundaries.

For simplicity reasons again, in particular to provide the simplest possible link with classical dimensionless numbers, we have ignored all prefactors. This can be a bit irritating when these prefactors pile up to produce orders of magnitude... For objects of particular interest, such as Earth's core and Sun's convective zone, it might be desirable to adopt a more accurate description.

We observe that density anomaly spectra from numerical simulations are rarely displayed, while they convey valuable information. We also note that spectra from laboratory experiments are scarce (but see Madonia et al. [2023]) and too often given in 'arbitrary units', preventing their conversion into  $\tau$ - $\ell$  representation. We are lacking experimental data on turbulence for rotating convection in a sphere in presence of strong magnetic fields.

$\tau$ - $\ell$  diagrams provide hints on how velocity and magnetic field scale with length-scale. This might be useful for observers who need such constraints to tune their magnetic field and core-flow inversions [Gillet et al., 2015, Baerenzung et al., 2016].

## 8. Conclusion

$\tau$ - $\ell$  regime diagrams are a simple graphical tool that proves useful for inventing or testing dynamic scenarios for planetary cores. Tradition in fluid dynamics is to characterize systems by dimensionless numbers, usually based on 'typical' large-scale quantities. Past decades have seen large efforts to develop a more detailed description of phenomena that operate at different scales. This has led to the apparition of even more dimensionless numbers, in which the various scales involved do not always figure very clearly, and to the construction of somewhat unintelligible scaling laws. By defining  $\tau$  timescales that depend on  $\ell$  length-scales over their entire range, we hope to make these choices more explicit. By providing a simple graphical identity to these scales, we wish to make their meaning more intuitive. Contrary to spectra in 'arbitrary units',  $\tau$ - $\ell$  diagrams give insight into regimes and balances which are paramount to rotating, magnetized and/or stratified fluids, where waves can be present and significantly alter the dynamics.

Because they put together most key properties of a given object,  $\tau$ - $\ell$  regime diagrams constitute a nice identity card. We think this applies to numerical simulations and laboratory experiments as well. Both approaches enable extensive parameter surveys, which are crucial for exploring and understanding different regimes. Being object-oriented,  $\tau$ - $\ell$  diagrams are not easily applied to such surveys, but we think they would very valuably complement classical scaling law plots. The idea would be to draw  $\tau$ - $\ell$  diagrams for a few representative members and end-members of the survey, which would nicely illustrate their validity range.

Our article thus has two goals. The first goal is to provide all ingredients for building your own  $\tau$ - $\ell$  diagram, be it of a numerical simulation, a laboratory experiment or theory. To that end, we included construction rules, examples, technical appendices, and Python scripts (supplementary material). The second goal is to demonstrate the potential of  $\tau$ - $\ell$  regime diagrams for suggesting and testing various scenarios for Earth's dynamo.

Convinced that available convective power  $\mathcal{P}_{diss}$  is a key control parameter, and the one that can most readily be estimated for other planets and exoplanets, we have modified our original approach [Nataf and Schaeffer, 2015] to propose and discuss a few scenarios built upon this input data. This results in a more challenging exercise, calling for force balance inspection.

The resulting  $\tau$ - $\ell$  diagrams (Figures 4b, 5a, 5b) display more clearly than previous analyses the range of validity of assumed force balances. In particular, a diversion to Venus (Figure 6) calls for a re-analysis of what is called a ‘fast rotator’.

## Conflicts of interest

The authors declare no competing financial interest.

## Dedication

The manuscript was mostly written by HCN. NS ran all presented numerical simulations. Both authors have given approval to the final version of the manuscript.

## Acknowledgments

We thank the French Academy of Science and Electricité de France for granting their “Ampère Prize” to our “Geodynamo” team, and Bérengère Dubrulle for early encouragements. HCN thanks Peter Davidson, Emmanuel Dormy, Julien Aubert, Thomas Gastine and Franck Plunian for useful discussions. The authors would like to thank the Isaac Newton Institute for Mathematical Sciences, Cambridge, for support and hospitality during the programme “Frontiers in dynamo theory: from the Earth to the stars” where work on this paper was undertaken. This work was supported by EPSRC grant no EP/R014604/1. ISTERre is part of Labex OSUG@2020 (ANR10 LABX56).

## Supplementary data

Supplementary material is available in document Nataf\_Schaeffer\_SupMat.pdf. All Python scripts and data used to produce the figures of this article are available in package tau-ell\_programs.zip at article’s URL and at [https://gricad-gitlab.univ-grenoble-alpes.fr/natafh/tau-ell\\_programs](https://gricad-gitlab.univ-grenoble-alpes.fr/natafh/tau-ell_programs).

## Appendix A. $\tau$ - $\ell$ representation of turbulent spectra

Our ‘fuzzy physics’ approach targets gathering dominant physical phenomena in a common frame. Some of them are classically defined in wavenumber or frequency space, rather than in physical space, hence the need for some conversion. This appendix lists the different types of energy spectra that are usually obtained from observations, numerical simulations and experiments, and derives recipes for converting them into  $\tau$ - $\ell$  language.

### A.1. Choosing a conversion rule

We consider different expressions of total energy per unit mass  $\mathcal{U}$ :

$$\mathcal{U} = \int E(k)dk \quad \text{or} \quad \mathcal{U} = \sum_{k_i} E_B(k_i) \quad \text{or} \quad \mathcal{U}(r) = \sum_n \mathcal{L}_n(r). \quad (32)$$

$E(k)$  is the classical *spectral energy density* introduced by Kolmogorov [1941].  $E_B(k_i)$  is the discrete equivalent of  $E(k)$  for flow ‘in a box’ [Lesieur, 2008].  $\mathcal{L}_n(r)$  is the degree  $n$  component at radius  $r$  of Lowes-Mauersberger spectrum widely used in geomagnetism [Loves, 1966].

A flow with spectral energy density  $E(k) \propto k^{-5/3}$  yields the same  $k$ -exponent for its discrete energy spectrum  $E_B$  [Lesieur, 2008, Stepanov et al., 2014], and a  $n^{-5/3}$  Lowes-Mauersberger spectrum. However, pre-factors may differ. More importantly, the conversion of energy spectra into  $\tau$ - $\ell$  equivalents is questionable.

In Kolmogorov [1941]'s universal turbulence, an *eddy turnover time* is classically derived as:

$$\tau_u(\ell) \simeq \ell^{3/2} [E(k)]^{-1/2} \quad \text{with} \quad \ell \simeq 1/k, \quad (33)$$

where  $\ell$  is the 'size' of the eddy. A similar result is obtained using *velocity increments*  $S_2(\ell) = \langle [u(x+\ell) - u(x)]^2 \rangle$ . This conversion rule was used in Nataf and Schaeffer [2015], and we kept it to build Figure 1. This approach is appealing for Kolmogorov-type self-similar inertial range where no length-unit other than  $\ell$  should appear, and where large eddies are more energetic than small eddies. Even then, no exact conversion between spectral energy density and eddy velocity can be drawn, as thoroughly discussed by Davidson and Pearson [2005].

In this article, we prefer converting spectral harmonic coefficients of energy at a given degree  $n$  into velocity or magnetic field at the scale corresponding to  $n$ . Equation (33) is then replaced by:

$$\tau_u(\ell(n)) \simeq \ell(n) [\mathcal{L}_n]^{-1/2} \quad \text{with} \quad \ell(n) \simeq \frac{1}{2} \frac{\pi R_o}{n + 1/2}. \quad (34)$$

## A.2. Application to various relevant spectra

We now detail the  $\tau$ - $\ell$  conversion of spectra commonly obtained from observations, numerical experiments and laboratory experiments/

### A.2.1. Lowes-Mauersberger spectrum

In geomagnetism, the variation of magnetic energy with length-scale is usually measured by its Lowes-Mauersberger spectrum [Lowes, 1966]. This spectrum is expressed in terms of Gauss coefficients  $g_n^m$  and  $h_n^m$  of scalar magnetic potential  $V$ , which defines the internal magnetic field at any radius above the core-mantle boundary when the mantle is considered as an electrical insulator.

Potential  $V(r, \theta, \varphi)$  is then solution of Laplace equation and can be expressed in terms of spherical harmonics as:

$$V(r, \theta, \varphi) = R_o \sum_{n=1}^{\infty} \sum_{m=0}^n \left( \frac{R_o}{r} \right)^{n+1} (g_n^m \cos m\varphi + h_n^m \sin m\varphi) P_n^m(\cos \theta), \quad (35)$$

where  $P_n^m$  are the Schmidt semi-normalized associated Legendre functions of degree  $n$  and order  $m$  (note that the spherical harmonic degree is often noted  $l$  rather than  $n$ , which we have adopted to avoid a confusion with length-scale  $\ell$ ).

Following Langlais et al. [2014], the Lowes-Mauersberger spectrum at any  $r > R_o$  is then given by the suite of  $\mathcal{L}_n$  defined by:

$$\mathcal{L}_n(r) = (n+1) \sum_{m=0}^n ((g_n^m)^2 + (h_n^m)^2) \left( \frac{R_o}{r} \right)^{2n+4}. \quad (36)$$

The total magnetic energy per unit mass at radius  $r$  is obtained as:

$$\mathcal{U}_m(r) \equiv \frac{B^2(r)}{2\mu} = \sum_{n=1}^{\infty} \mathcal{L}_n(r). \quad (37)$$

Spherical harmonic degree  $n$  is related to our  $\ell$  length-scale by:

$$\ell(n) \simeq \frac{1}{2} \frac{\pi R_o}{n + 1/2}. \quad (38)$$

We deduce from equations (37) and (38) that the magnetic field  $b(\ell, r)$  at length-scale  $\ell$  and radius  $r$  is given by:

$$b(\ell(n), r) \simeq \sqrt{2\mu \mathcal{L}_n(r)}. \quad (39)$$

We finally obtain  $\tau_b(\ell)$  from:

$$\tau_b(\ell(n)) \simeq \frac{\ell(n)}{\sqrt{2\mathcal{L}_n(r)\rho}} \quad \text{with} \quad \ell(n) = \frac{1}{2} \frac{\pi R_o}{n + 1/2}. \quad (40)$$

A flat Lowes-Mauersberger spectrum (constant  $\mathcal{L}_n$ ), such as observed for the Earth's magnetic field at the core-mantle boundary, thus translates into  $\tau_b(\ell) \propto \ell$ .



### A.2.2. Numerical simulation spectra

Numerical simulations of planetary dynamos are most often performed using a pseudo-spectral expansion in spherical harmonics  $Y_n^m(\theta, \varphi)$  of degree  $n$  and order  $m$ . Degree- $n$  or order- $m$  spectra are thus readily obtained for both velocity, magnetic and codensity fields. These spectra are usually for  $u^2$ ,  $b^2$  and  $C^2$  in dimensionless units, such that the sum over all  $n$  and  $m$  yields  $2/\rho$  times the energy per unit mass of that dimensionless field. Given length-scale  $L$  and time-scale  $T$  chosen in the simulation,  $u$  and  $b$  spectra should be multiplied by  $L^2/T^2$  (assuming that  $b$  is expressed in Alfvén wave velocity units).

### A.2.3. Degree- $n$ energy spectra

Given these precisions, the procedure is similar to that exposed in section A.2.1.  $\ell(n)$  is given by:

$$\ell(n) = \frac{1}{2} \frac{\pi R_o}{n + 1/2}. \quad (41)$$

One should keep in mind that for a given degree  $n$ , the corresponding length-scale varies linearly with radius. This is ignored in our approach. If  $\mathcal{S}_n$  is the  $n$ -element of the dimensionless  $x^2$  spectrum, then the corresponding  $\tau_x(\ell)$  lines for  $x = u, b$  and  $\rho$  are given by:

$$\tau_u(\ell(n)) \simeq \frac{T}{L} \frac{\ell(n)}{\sqrt{\mathcal{S}_n}}, \quad (42)$$

$$\tau_b(\ell(n)) \simeq \frac{T}{L} \frac{\ell(n)}{\sqrt{\mathcal{S}_n}}, \quad (43)$$

$$\tau_\rho(\ell(n)) \simeq \sqrt{\frac{\ell(n)}{g \sqrt{\mathcal{S}_n}}}, \quad (44)$$

where gravity  $g$  (in dimensional units) is obtained from the input Rayleigh number.

In the example of Figure 3a from Guervilly et al. [2019], the simulated acceleration of gravity  $g$  at the top boundary is obtained from:

$$g = \frac{\text{Ra} R_o \kappa \nu}{R_o^4}, \quad (45)$$

with  $\text{Ra} = 2.5 \times 10^{10}$ .

In the example of Figure 4a from Schaeffer et al. [2017],  $g$  is obtained from:

$$g = \frac{\text{Ra}^* R_o \kappa \nu}{(R_o - R_i)^4}, \quad (46)$$

with  $\text{Ra}^* = \text{Ra} / \beta R_o = 2.4 \times 10^{13}$ , where  $\beta$  is the imposed codensity gradient at the top boundary. We then obtain the  $\tau_\rho(\ell)$  line by applying equation (44) to the codensity spectrum multiplied by  $\text{Pr}^2$ .

### A.2.4. Order- $m$ energy spectra

Quasi-geostrophic vortices are better characterized by their order- $m$  spectra  $\mathcal{S}_m$  than by their degree- $n$  spectra, in particular in 2D QG simulations. Thus Guervilly et al. [2019] display  $m$ -spectra of their 3D and QG convection simulation results. Translation into  $\tau$ - $\ell$  is obtained as in Appendix A.2.3, replacing  $\mathcal{S}_n$  by  $\mathcal{S}_m$ . For the simulation presented in Figure 3a,  $\mathcal{S}_m$  and  $\mathcal{S}_n$  spectra are very similar, apart for even-odd oscillations in the  $n$ -spectra due to equatorial symmetry.

### A.2.5. Frequency spectrum

In laboratory experiments, turbulent spectra are more easily obtained from signal  $x(\mathbf{r}, t)$  measured in the time-domain ( $t = 0$  to  $T$ ) at a given position  $\mathbf{r}$ . Power spectral density (PSD) is then computed from its Fourier transform  $\hat{x}_T(\mathbf{r}, f)$  as:

$$\tilde{E}(\mathbf{r}, f) = \lim_{T \rightarrow \infty} \frac{1}{T} |\hat{x}_T(\mathbf{r}, f)|^2. \quad (47)$$

When a mean flow  $\mathbf{U}(\mathbf{r})$  is present, and when turbulence is weak enough, a time record reflects advection of the spatial variation of velocity [e.g., Frisch, 1995]. Extensions to intense turbulence have been developed [Pinton and Labbé, 1994]. Taylor's hypothesis [Taylor, 1938] then permits to obtain a kinetic energy density wavenumber spectrum  $E(\mathbf{r}, k)$  from the velocity frequency power spectrum  $\tilde{E}(\mathbf{r}, f)$ :

$$E(\mathbf{r}, k(f)) = \frac{U}{2\pi} \tilde{E}(\mathbf{r}, f) \quad \text{with} \quad k(f) = \frac{2\pi f}{U}, \quad (48)$$

where  $U = \|\mathbf{U}(\mathbf{r})\|$ . Strictly speaking, this is a  $k_{//}$ -spectrum, valid for wavenumber  $\mathbf{k}$  parallel to mean velocity vector  $\mathbf{U}(\mathbf{r})$ . It is the same as a  $k$ -spectrum for isotropic turbulence. The  $\tau$ - $\ell$  translation is then obtained from equation (40).

Note that Taylor's hypothesis cannot be applied to magnetic spectra unless magnetic diffusion is small enough for the frozen flux approximation to apply.

### A.3. Dissipation in $\tau$ - $\ell$ diagrams

One advantage of using equation (34) for converting spectra into  $\tau$ - $\ell$  lines is that dissipation is maximum at the minimum time.

In discrete series from numerical simulations, total viscous dissipation per unit mass is estimated from:

$$\epsilon_v = 2\nu \sum_{\ell} \frac{1}{\tau_u^2(\ell)}. \quad (49)$$

This equation confirms that maximum dissipation per unit mass is attained at minimum  $\tau_u(\ell_*) = \tau_{min}$ , where it can be approximated by:

$$\tilde{\epsilon}_v = \frac{2\nu}{\tau_{min}^2} \quad (50)$$

(remember that our fuzzy approach ignores  $\mathcal{O}(1)$  prefactors).

We have estimated viscous (and Ohmic) dissipation from sum (49) applied to lines  $\tau_u(\ell)$  of  $\tau$ - $\ell$  diagram of Guervilly et al. [2019]'s 3D simulation shown in Figure 3a, and to lines  $\tau_u(\ell)$  and  $\tau_b(\ell)$  of S2 DNS of Schaeffer et al. [2017] displayed in Figure 4a. Obtained values (dotted lines) compare well with actual simulation results (dashed lines), but plot at least a factor of 10 below corresponding  $\tau_{min}$  times.

## Appendix B. Force balances in $\tau$ - $\ell$ diagrams

In this Appendix, we present the dominant force balances expected in planetary cores, and derive their  $\tau$ - $\ell$  translation.

Let us start from the Navier-Stokes equation for deviations from hydrostatic equilibrium in an incompressible fluid under the Boussinesq approximation:

$$\rho (\partial_t \mathbf{u} + \mathbf{u} \cdot \nabla \mathbf{u} + 2\Omega \times \mathbf{u}) = -\nabla p + \Delta \rho \mathbf{g} + \mathbf{j} \times \mathbf{b} + \rho \nu \nabla^2 \mathbf{u}, \quad (51)$$

where the symbols have their usual meaning: velocity  $\mathbf{u}$ , pressure  $p$ , electric current density  $\mathbf{j}$ , magnetic field  $\mathbf{b}$ . The acceleration term on the left-hand side includes advection and Coriolis, while the right-hand side figures pressure gradient, buoyancy, Lorentz, and viscous forces.

Following Aubert [2019], Schwaiger et al. [2019], Schwaiger [2020], we consider five types of force balances: QG, CIA, QG-CIA, MAC and QG-MAC.

### B.1. Leading-order Quasi-Geostrophy (QG)

When Coriolis is the dominant acceleration, one gets geostrophic equilibrium:

$$2\rho\Omega \times \mathbf{u} = -\nabla p, \quad (52)$$

Taking the curl of this equation yields *Proudman-Taylor constraint*:

$$\frac{\partial \mathbf{u}}{\partial z} = 0, \quad (53)$$

where  $z$  coordinate is parallel to  $\Omega$ .

At next order, Proudman-Taylor constraint implies that the projection of velocity gradient along the spin axis  $(\Omega \cdot \nabla) \mathbf{u}$  is small, scaling as  $1/\ell_{\parallel}$ , where  $\ell_{\parallel} \sim R_o$  [Julien et al., 2012].

### B.2. Coriolis-Inertia-Archimedean (CIA)

Consider the three-term balance of Coriolis, inertia and Archimedean forces. At a given length-scale  $\ell_{\perp}$ , retaining these forces in the curl of equation (51) yields:

$$\frac{\Omega u}{\ell_{\perp}} \sim \frac{u^2}{\ell_{\perp}^2} \sim \frac{\Delta \rho}{\rho} \frac{g}{\ell_{\perp}} \quad (54)$$

Translating in  $\tau$ - $\ell$  language, we get:

$$t_{\Omega} \tau_u(\ell_{\perp}) \sim \tau_u^2(\ell_{\perp}) \sim \tau_{\rho}^2(\ell_{\perp}), \quad (55)$$

which implies:

$$\tau_u(\ell_{\perp}) \sim t_{\Omega} \sim \tau_{\rho}(\ell_{\perp}). \quad (56)$$

This is the regime we expect when the  $\tau_u(\ell)$  line reaches the  $t_{\Omega}$  line, where  $\text{Ro}(\ell_{\perp}) \sim 1$ .

### B.3. Quasi-Geostrophic Coriolis-Inertia-Archimedean (QG-CIA)

Quasi-geostrophy applies at leading order when Coriolis largely dominates over inertia ( $\text{Ro} \ll 1$ ), if other forces are small as well. Fluid motions are organized in columnar eddies aligned with the spin axis. Dynamics of these convective columns can still be controlled by a (quasi-geostrophic) CIA balance, in which the Coriolis term is reduced to its ageostrophic part:

$$\frac{\Omega u}{\ell_{\parallel}} \sim \frac{u^2}{\ell_{\perp}^2} \sim \frac{\Delta \rho}{\rho} \frac{g}{\ell_{\perp}} \quad (57)$$

The first term corresponds to vortex stretching, the second one to vorticity advection, and the last one to vortex generation by buoyancy (see Cardin and Olson [1994], Jones [2015]).

Translating in  $\tau$ - $\ell$  language, we get:

$$t_{\Omega} \tau_u(\ell_{\parallel}) \sim \tau_u^2(\ell_{\perp}) \sim \tau_{\rho}^2(\ell_{\perp}). \quad (58)$$

### B.4. Magneto-Archimedean-Coriolis (MAC)

When magnetic Lorentz force is strong enough to break quasi-geostrophy at scale  $\ell_{\perp}$ , one can get a balance between Lorentz, buoyancy and Coriolis forces, such that:

$$\frac{\Omega u}{\ell_{\perp}} \sim \frac{b^2}{\rho \mu \ell_{\perp}^2} \sim \frac{\Delta \rho}{\rho} \frac{g}{\ell_{\perp}}, \quad (59)$$

analogous to the CIA balance with fluid velocity replaced by Alfvén wave velocity in the advection term. Translating in  $\tau$ - $\ell$  language, we get:

$$t_{\Omega} \tau_u(\ell_{\perp}) \sim \tau_b^2(\ell_{\perp}) \sim \tau_{\rho}^2(\ell_{\perp}), \quad (60)$$

which implies:

$$\Lambda(\ell_{\perp}) = \frac{t_{\Omega} \tau_u(\ell_{\perp})}{\tau_b^2(\ell_{\perp})} \sim 1. \quad (61)$$

This is the regime we get when the magnetic field is strong enough (see Aurnou and King [2017]). The Elsasser number (sometimes called dynamical Elsasser number, noted  $\Lambda_d$ ) is of order one at scale  $\ell_{\perp}$ .

### B.5. Quasi-Geostrophic Magneto-Archimedean-Coriolis (QG-MAC)

When leading order force balance is quasi-geostrophic, the Coriolis term should only involve its ageostrophic part, at a length-scale  $\ell_{\parallel} \sim R_o$ . QG-MAC balance therefore writes:

$$\frac{\Omega u}{\ell_{\parallel}} \sim \frac{b^2}{\rho \mu \ell_{\perp}^2} \sim \frac{\Delta \rho}{\rho} \frac{g}{\ell_{\perp}}, \quad (62)$$

analogous to the QG-CIA balance with fluid velocity replaced by Alfvén wave velocity in the advection term. Translating in  $\tau$ - $\ell$  language, we get:

$$t_{\Omega} \tau_u(\ell_{\parallel}) \sim \tau_b^2(\ell_{\perp}) \sim \tau_{\rho}^2(\ell_{\perp}), \quad (63)$$

## References

- Alemanly, A., Moreau, R., Sulem, P., and Frisch, U. (1979). Influence of an external magnetic field on homogeneous MHD turbulence. *Journal de Mécanique*, 18, 277–313.
- Alfvén, H. (1942). Existence of electromagnetic-hydrodynamic waves. *Nature*, 150(3805), 405–406. <https://doi.org/10.1038/150405d0>.
- Aubert, J. (2013). Flow throughout the Earth’s core inverted from geomagnetic observations and numerical dynamo models. *Geophysical Journal International*, 192(2), 537–556. <https://doi.org/10.1093/gji/ggs051>, <https://arxiv.org/abs/https://academic.oup.com/gji/article-pdf/192/2/537/5940031/ggs051.pdf>.
- Aubert, J. (2019). Approaching Earth’s core conditions in high-resolution geodynamo simulations. *Geophysical Journal International*, 219(Supplement\_1), S137–S151.
- Aubert, J., Gastine, T., and Fournier, A. (2017). Spherical convective dynamos in the rapidly rotating asymptotic regime. *Journal of Fluid Mechanics*, 813, 558–593.
- Aurnou, J. and King, E. (2017). The cross-over to magnetostrophic convection in planetary dynamo systems. *Proceedings of the Royal Society A: Mathematical, Physical and Engineering Sciences*, 473(2199), 20160731.
- Baerenzung, J., Holschneider, M., and Lesur, V. (2016). The flow at the Earth’s core-mantle boundary under weak prior constraints. *Journal of Geophysical Research: Solid Earth*, 121(3), 1343–1364.
- Cardin, P. and Olson, P. (1994). Chaotic thermal convection in a rapidly rotating spherical shell: consequences for flow in the outer core. *Physics of the earth and planetary interiors*, 82(3-4), 235–259.
- Cattaneo, F. and Hughes, D. W. (2022). How was the Earth–Moon system formed? new insights from the geodynamo. *Proceedings of the National Academy of Sciences*, 119(44), e2120682119.
- Christensen, U. (2010). Dynamo scaling laws and applications to the planets. *Space science reviews*, 152(1), 565–590.
- Christensen, U. and Aubert, J. (2006). Scaling properties of convection-driven dynamos in rotating spherical shells and application to planetary magnetic fields. *Geophys. J. Int.*, 166(1), 97–114.
- Christensen, U., Olson, P., and Glatzmaier, G. (1999). Numerical modelling of the geodynamo: a systematic parameter study. *Geophysical Journal International*, 138(2), 393–409.
- Christensen, U. R., Aubert, J., and Hulot, G. (2010). Conditions for Earth-like geodynamo models. *Earth and Planetary Science Letters*, 296(3-4), 487–496.
- Davidson, P. (2013). Scaling laws for planetary dynamos. *Geophysical Journal International*, 195(1), 67–74.
- Davidson, P. (2014). The dynamics and scaling laws of planetary dynamos driven by inertial waves. *Geophysical Journal International*, 198(3), 1832–1847.
- Davidson, P. and Pearson, B. (2005). Identifying turbulent energy distributions in real, rather than Fourier, space. *Physical review letters*, 95(21), 214501.
- Davidson, P. A., Staplehurst, P. J., and Dalziel, S. B. (2006). On the evolution of eddies in a rapidly rotating system. *Journal of Fluid Mechanics*, 557, 135–144.
- Dormy, E. (2016). Strong-field spherical dynamos. *Journal of Fluid Mechanics*, 789, 500–513.

- Driscoll, P. and Davies, C. (2023). The “new core paradox”: Challenges and potential solutions. *Journal of Geophysical Research: Solid Earth*, 128(1), e2022JB025355. <https://agupubs.onlinelibrary.wiley.com/doi/abs/10.1029/2022JB025355>, <https://arxiv.org/abs/https://agupubs.onlinelibrary.wiley.com/doi/pdf/10.1029/2022JB025355>, e2022JB025355 2022JB025355.
- Frisch, U. (1995). *Turbulence: the legacy of A.N. Kolmogorov*. Cambridge University Press.
- Gastine, T., Wicht, J., and Aubert, J. (2016). Scaling regimes in spherical shell rotating convection. *Journal of Fluid Mechanics*, 808, 690–732.
- Gillet, N., Jault, D., Canet, E., and Fournier, A. (2010). Fast torsional waves and strong magnetic field within the Earth’s core. *Nature*, 465(7294), 74–77. <https://doi.org/10.1038/nature09010>.
- Gillet, N., Jault, D., and Finlay, C. (2015). Planetary gyre, time-dependent eddies, torsional waves, and equatorial jets at the Earth’s core surface. *Journal of Geophysical Research: Solid Earth*, 120(6), 3991–4013.
- Gillet, N. and Jones, C. (2006). The quasi-geostrophic model for rapidly rotating spherical convection outside the tangent cylinder. *Journal of Fluid Mechanics*, 554, 343–369.
- Glatzmaier, G. A. and Roberts, P. H. (1995). A three-dimensional self-consistent computer simulation of a geomagnetic field reversal. *Nature*, 377, 203–+.
- Greenspan, H. P. (1968). *The theory of rotating fluids*. CUP Archive.
- Guervilly, C., Cardin, P., and Schaeffer, N. (2019). Turbulent convective length scale in planetary cores. *Nature*, 570(7761), 368–371.
- Guzmán, A. J. A., Madonia, M., Cheng, J. S., Ostilla-Mónico, R., Clercx, H. J., and Kunnen, R. P. (2021). Force balance in rapidly rotating Rayleigh–Bénard convection. *Journal of fluid mechanics*, 928, A16.
- Jault, D. (2008). Axial invariance of rapidly varying diffusionless motions in the Earth’s core interior. *Phys. Earth Planet. Inter.*, 166, 67–76.
- Jones, C. A. (2015). *Treatise on Geophysics*, volume 8, Core Dynamics, chapter 8.05, Thermal and compositional convection in the outer core, pages 115–159. Elsevier BV, second edition.
- Julien, K., Rubio, A. M., Grooms, I., and Knobloch, E. (2012). Statistical and physical balances in low Rossby number Rayleigh–Bénard convection. *Geophysical & Astrophysical Fluid Dynamics*, 106(4-5), 392–428.
- Kageyama, A., Sato, T., and Complexity Simulation Group (1995). Computer simulation of a magnetohydrodynamic dynamo. ii. *Physics of Plasmas*, 2(5), 1421–1431.
- Kaplan, E., Nataf, H.-C., and Schaeffer, N. (2018). Dynamic domains of the Derviche Tourneur sodium experiment: Simulations of a spherical magnetized Couette flow. *Physical Review Fluids*, 3(3), 034608.
- Kolmogorov, A. (1941). The local structure of turbulence in incompressible viscous fluid for very large Reynolds number. *Dokl. Akad. Nauk. SSSR*, 30, 9–13.
- Landeau, M., Fournier, A., Nataf, H.-C., Cébron, D., and Schaeffer, N. (2022). Sustaining Earth’s magnetic dynamo. *Nature Reviews Earth & Environment*, 3(4), 255–269.
- Langlais, B., Amit, H., Larnier, H., Thébault, E., and Mocquet, A. (2014). A new model for the (geo) magnetic power spectrum, with application to planetary dynamo radii. *Earth and Planetary Science Letters*, 401, 347–358.
- Lehnert, B. (1954). Magnetohydrodynamic waves under the action of the Coriolis force. *The Astrophysical Journal*, 119, 647.
- Lesieur, M. (2008). *Turbulence in fluids*, volume 84 of *Fluid Mechanics and its Applications*. Springer, fourth edition edition.
- Lister, J. R. (2003). Expressions for the dissipation driven by convection in the Earth’s core. *Physics of the Earth and Planetary Interiors*, 140(1-3), 145–158.
- Loves, F. (1966). Mean-square values on sphere of spherical harmonic vector fields. *Journal of Geophysical Research*, 71(8), 2179–2179.
- Madonia, M., Guzmán, A. J. A., Clercx, H. J., and Kunnen, R. P. (2023). Reynolds number scaling and energy spectra in geostrophic convection. *Journal of Fluid Mechanics*, 962, A36.
- Nataf, H.-C. and Gagnière, N. (2008). On the peculiar nature of turbulence in planetary dynamos. *Comptes Rendus Physique*, 9(7), 702–710.

- Nataf, H.-C. and Schaeffer, N. (2015). *Treatise on Geophysics*, volume 8, Core Dynamics, chapter 8.06, Turbulence in the core, pages 161–181. Elsevier BV, second edition.
- Nimmo, F. (2002). Why does Venus lack a magnetic field? *Geology*, 30(11), 987–990.
- Nimmo, F. (2015). *Treatise on Geophysics*, volume 8, Core Dynamics, chapter 8.02, Energetics of the core, pages 27–55. Elsevier BV, second edition.
- Olson, P. (2015). *Treatise on Geophysics*, volume 8, Core Dynamics, chapter 8.01, Core dynamics: an introduction and overview, pages 1–25. Elsevier BV, second edition.
- Olson, P. and Christensen, U. R. (2006). Dipole moment scaling for convection-driven planetary dynamos. *Earth and Planetary Science Letters*, 250(3-4), 561–571.
- Pais, M. and Jault, D. (2008). Quasi-geostrophic flows responsible for the secular variation of the Earth's magnetic field. *Geophysical Journal International*, 173(2), 421–443.
- Pinton, J. and Labbé, R. (1994). Correction to the Taylor hypothesis in swirling flows. *J. Phys. II France*, 4(9), 1461–1468. <https://doi.org/10.1051/jp2:1994211>.
- Rhines, P. B. (1975). Waves and turbulence on a beta-plane. *Journal of Fluid Mechanics*, 69(3), 417–443.
- Russell, C. T. (1980). Planetary magnetism. *Reviews of Geophysics*, 18(1), 77–106.
- Schaeffer, N., Jault, D., Nataf, H.-C., and Fournier, A. (2017). Turbulent geodynamo simulations: a leap towards Earth's core. *Geophysical Journal International*, 211(1), 1–29.
- Schwaiger, T. (2020). *Geodynamo simulations in the Earth's core dynamical regime : a systematic study*. Theses, Université Paris Cité, <https://theses.hal.science/tel-03344030>.
- Schwaiger, T., Gastine, T., and Aubert, J. (2019). Force balance in numerical geodynamo simulations: a systematic study. *Geophysical Journal International*, 219(Supplement\_1), S101–S114.
- Stepanov, R., Plunian, F., Kessar, M., and Balarac, G. (2014). Systematic bias in the calculation of spectral density from a three-dimensional spatial grid. *Physical Review E*, 90(5), 053309.
- Stevenson, D. J., Spohn, T., and Schubert, G. (1983). Magnetism and thermal evolution of the terrestrial planets. *Icarus*, 54(3), 466–489.
- Taylor, G. I. (1938). The spectrum of turbulence. *Proceedings of the Royal Society of London. Series A-Mathematical and Physical Sciences*, 164(919), 476–490.
- Teed, R. J. and Dormy, E. (2023). Solenoidal force balances in numerical dynamos. *Journal of Fluid Mechanics*, 964, A26.
- Yan, M. and Calkins, M. A. (2022). Asymptotic behaviour of rotating convection-driven dynamos in the plane layer geometry. *Journal of Fluid Mechanics*, 951, A24.